Title
Processing and Properties of High Performance Lead Free Electro-Optic Ceramics

Author
Dupuy, Alexander Davis

Publication Date
2016

UNIVERSITY OF CALIFORNIA
RIVERSIDE

Processing and Properties of High Performance Lead Free Electro-Optic Ceramics

A Dissertation submitted in partial satisfaction
of the requirements for the degree of

Doctor of Philosophy

in

Mechanical Engineering

by

Alexander Davis Dupuy

August 2016

Dissertation Committee
    Dr. Javier Garay, Chairperson
    Dr. Yasuhiro Kodera
    Dr. Masaru P. Rao

The Dissertation of Alexander Davis Dupuy is approved:

Committee Chairperson

University of California, Riverside

Acknowledgements

I began my research career as a freshman in the spring of 2006. There have been a lot of ups and downs throughout my time as a student. Although I have made many mistakes during my career, I am extremely proud of what I have accomplished here at UCR. I now stand at the precipice of the rest of my career, ready to face the challenges that are ahead of me. When I wrote my Masters thesis in 2011, I left this section blank. At that time I lacked the hindsight and maturity to admit that there were people who had helped me along the way. No one can get a doctorate by themselves, and I know now that I have a lot of people to thank for helping me during this long emotional journey.

The most obvious place to begin my acknowledgements is with my advisor Javier Garay. Volumes could be written about our relationship and his impact on the man that I am today. For the purposes of brevity, I will focus on what I believe to be the most meaningful aspects of being mentored by him for the last ten years. When I stumbled into Dr. Garay's lab for the first time I was a clumsy immature freshman with no useful experience in anything related to engineering. I certainly had no business being in a research lab. Dr. Garay showed an immense amount of trust and confidence in me from the first day. The trust he showed me and the freedom he provided me have literally changed my life. The work I am presenting in my dissertation is the result of several slow agonizing years of hard work. There were probably many times when Dr. Garay wanted to strangle me because of how stubborn I was being. Despite this he was patient with me and gave me the freedom to solve my problems in my own way. His trust and patience ultimately paid off in the end, and for that I am extremely thankful.

I am also very thankful for my second mentor, Dr. Yasuhiro Kodera. Yasu came to our lab at a pivotal time for me. Dr. Garay was becoming very busy and was relying on me to be the lab manager. I, however, was not a fully cooked researcher yet. I was still in need of mentorship, and Yasu was able to provide that for me. He showed me a different perspective on my research and opened my eyes to many other forms of problem solving that I would not have gotten anywhere else. Yasu has also been my culinary mentor. When I met Yasu, I ate food that primarily reflected my Midwest and east coast heritage. I will always very fondly remember our trips to the "west" where we would spend hours on the weekends finding obscure restaurants. Thanks to Yasu I can now eat almost anything from almost anywhere.

I am eternally grateful for the support I received from Jason Morales. Jason came into my life early on in my research career. He became something of a role model and confidant for me while he was at UCR. Jason understood that no matter how many responsibilities and titles I was given, deep down I was still just a kid trying to find my place in the world. He always treated me with the respect that an adult and a colleague deserved. When I needed it, however, he was willing to help me navigate the trickier aspects of adulthood that I so often found myself unprepared for. He did this all while never making me feel bad or childish.

I also need to thank the second Jason in my life, Jason McMillan. Jason started working for me in the fall of 2010. At this time I was teaching, starting a new project, preparing for a conference, and I had just started my job as lab manager. I was completely overwhelmed and in over my head (although I tried not to show it). Jason and

I became an unstoppable team. I never needed to worry about the quality or timeliness of his work. Whether it was to help work or simply to bounce ideas off of, he was always there for me. My survival and success in the early part of graduate school was largely due to the support and assistance of Jason McMillan.

Although we have not always seen eye to eye, I need to thank Elias Penilla for his help in refining me into the researcher that I am today. Elias and I are both very stubborn, and we locked horns many times in graduate school. Elias, however, was one of the few people in my life willing and able to challenge me when my ego was getting the better of me. At the time it was infuriating, but I am now grateful for his criticisms. Elias and I have also shared many similar experiences throughout graduate school. It has been important in the later years of my career to have someone that I could talk to about these experiences.

I think that it is important to thank Dr. Yasuhiro Hasegawa, for orchestrating my trip to Japan. Dr. Hasegawa allowed me to stay in Japan and work in his lab for several weeks toward the end of 2012. What started as a simple collaboration between two labs became one of the most important experiences of my life. My trip to Japan exposed me to a different culture, both socially and academically, that has had a powerful influence on me ever since. I would also like to thank the members of “Team Japan”; Masayuki Murata, Yusuke Saito, and Katsuhito Shirota. The three of them took incredible care of me during my time in Japan. One the best parts of my trip was meeting the three of them, and forging a friendship that I hope will last forever.

I am sincerely grateful for the friendship of Corey Hardin, Christian Bartolome, and Joshua Hockel. Although we have all gone our separate ways, I will never forget all the things we were able to accomplish together. I thrived in my bachelors because of the help and support that they provided me. Some of the most difficult challenges of my life were undertaken with them by my side. I still fondly (in hindsight) remember staying up all night with them working on homework assignments and projects because we were overachievers and had bitten off more than we could chew. Because we were a team, we were able to reach for the stars and achieve things that we could not have hoped to do on our own. Our hard work yielded wonderful results, as all four of us have graduated with an engineering doctorate from the University of California.

I would also like to thank my friends and lab mates in AMPS lab. Your friendship and support was greatly appreciated. In particular I would like to thank all of the undergraduate students that have worked with me: Jason McMillan, Martin Go, Adrian Gherman, Robert Smith, Justin Cortez, and Daniel Cataldi. One of the most profound and important parts of my graduate career has been watching all of you grow and develop as scientists. All of you have contributed something meaningful to my work, and for that I am sincerely thankful. My greatest hope is that everyone one of you was able to benefit from your research experience and that you thrive in whatever career you select for yourself.

I must of course acknowledge the love and support of my family. I know that this experience has been confusing for most of them. For the past ten years I have prioritized my career and I apologize for those in my family that I have hurt or ignored during that time. I sincerely appreciate your patience during this long journey of chasing my dreams. In particular I need to thank Mom and Matt for being my primary support during all of this. There is absolutely no way that I could have done any of this without the two of you. Despite your frequent apprehensions, you supported my career decisions every step of the way. I would also like to thank Sarah Nosce for being my muse throughout the last half of graduate school. Being at UCR gave us the opportunity to meet and for you to change my life for the better.

Last, but certainly not least, I need to thank the National Science Foundation for funding my work. Without the financial support of NSF my project would have been impossible. My project took an unusually long time to bear fruit, and the patience of my funders was greatly appreciated. This work was funded by an award from the Division of Materials Research of the National Science Foundation, grant number 0956071 with Dr. L. Madsen as program director. Some of the materials in my thesis were previously published in the following paper:

Dupuy, A. D., Kodera, Y. and Garay, J. E. (2016), Unprecedented Electro-Optic Performance in Lead-Free Transparent Ceramics. Adv. Mater..
doi:10.1002/adma.201600947

ABSTRACT OF THE DISERTATION

Processing and Properties of High Performance Lead Free Electro-Optic Ceramics

by

Alexander Davis Dupuy

Doctor of Philosophy, Graduate Program in Mechanical Engineering
University of California, Riverside, August 2016
Dr. Javier Garay, Chairperson

Electro-optic (EO) materials allow for the precise control of light using electrical signals, which has allowed for the advancement of an incredible array of photonic technologies such as laser systems and optical telecommunications. Most EO devices currently utilize single crystals, but high performance EO single crystals often have composition limitations since dopants can segregate and not all compositions can be grown using equilibrium restricted techniques. Bulk polycrystalline ceramic materials can potentially overcome such limitations and allow for the exploration of new EO systems. Due to the specific microstructures required for transparency, conventional processing techniques have difficulty in producing bulk polycrystalline EO ceramics. Reported here for the first time are the optical and EO properties of a new class of transparent lead free ceramic that outperforms EO materials in use today. This material is a barium titanate (BaTiO3) based solid solution, $(1\text{-}x)\mathrm{Ba(Zr0.2Ti0.8)O_3\text{-}x(Ba_{0.7}Ca_{0.3})TiO_3}$ referred to here as BXT. The EO material was successfully processed using the Current Activated Pressure Assisted Densification (CAPAD) technique, commonly called Spark Plasma Sintering (SPS), which has been shown to be effective at consolidating optical materials.

Using this technique along with a new powder synthesis method, it was possible to produce a transparent EO BXT ceramic with a highly dense and homogeneously reacted microstructure. Densified BXT shows a remarkable EO coefficient of 530 pm/V, which is superior not only to state of the art LiNbO3 crystals but also top-quality lead containing ferroelectric ceramics such as PLZT. This exceptional coefficient will allow for miniaturized EO systems with reduced operating voltages. The mechanisms behind the high EO performance in BXT were determined using additional EO and ferroelectric measurements. These measurements indicate that BXT undergoes a field induced structural evolution which heavily contributes to the EO effect. Along with efficient domain motion, this structural evolution includes a field induced phase change to a lower symmetry crystal structure. This work shows that lead free EO polycrystalline ceramics can have properties that are competitive or superior to state of the art EO materials. Due to its exceptional EO properties, BXT in particular has a promising future as an EO material.

Table of Contents

List of Figures

List of Tables

Chapter 1-Introduction

Technology which utilizes electromagnetic radiation has come to define the modern world. Much of the technology that dominates our culture makes use of microwave and radio wave frequencies. Light based technologies (commonly comprising the visible and near infrared wavelengths) are comparatively young, only being a few decades old. The impressive potential of this technology has allowed photonics industries to grow at an incredible pace. Photonic devices now find themselves in applications ranging from industrial manufacturing to medical devices.

Modern photonic systems require the precise control and manipulation of light. This is typically accomplished with electro-optic (EO) devices. These devices make use of materials with optical properties that are modifiable with electrical signals. At their most simple, EO devices can be categorized as optical switches or optical modulators (light valves). As seen in Figure 1.1, an optical switch is a device that turns on and off an external light source with an applied electrical signal. An optical modulator is a device that can vary the amount of light exiting the system by applying an appropriate voltage.

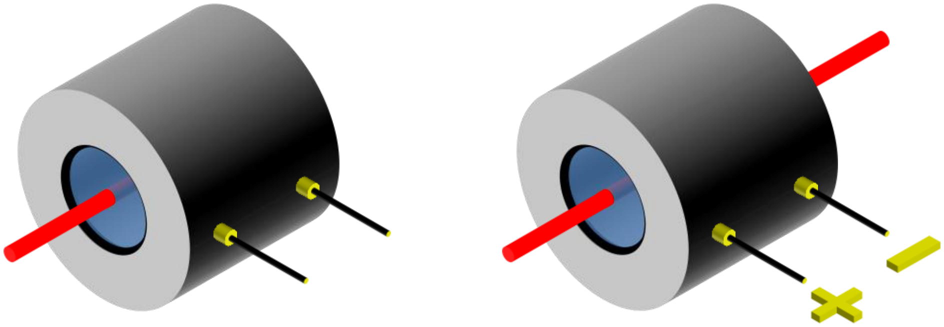

Figure 1.1: Schematic of an EO switch. When no signal is applied the incoming light is blocked. When the appropriate electric signal is applied the light can pass through the device.

1.1-Electro-Optic Devices

The most simple EO device in commercial use is an optical switch. These devices are used to simply turn on and off light. Their most common application is for data transfer in fiber optic telecommunication systems. A zero bit corresponds to the light being off, while a one bit corresponds to the light being on. EO devices are used in this application because of their speed. Ferroelectric based EO materials are popular for these applications because they can be modulated at Ghz frequencies, which are often demanded in high speed data networks.

EO devices are often found in laser systems. The systems frequently need external modulation to control the output intensity, necessitating an EO modulator. Higher power lasers also make use of a technique called Q-switching. This technique requires that an EO device be put into the cavity of a laser to manage the losses in the cavity. This allows the amount of energy stored in the laser to be carefully controlled while also controlling the pulse repetition rate. Q-switching allows for high energy light pulses at very high repetition rates. High power lasers making use of this technique can be found in industrial and medical lasers

1.2-Electro-Optic Materials

Currently, EO devices make heavy use of single crystal materials. Single crystals provide an exceptional level of transparency, even when large crystal sizes are necessary. Two of the most common single crystal materials are KH_2PO_4 (KDP) and $LiNbO_3$ (LN). LN in particular has found use in a large number of EO applications due to its stability. Despite their popularity, these single crystal materials do not have high EO efficiencies. This means that EO devices using these materials require high voltages and large (or multiple) crystals to operate. High performance single crystals are often prohibitively difficult to grow. For example $Pb(Mg_{1/2}Nb_{2/3})O_3$–$PbTiO_3$ (PMN-PT) crystals often suffer from compositional gradients formed during growth [1]. This can lead to dramatic differences in the EO performance across the length of the crystal [2].

Despite intense research, EO materials in thin film form have not been widely integrated into EO systems [3]. This is due to clamping effects interfering with the ferroelectric properties [4]. Such clamping effects are particularly severe in ferroelectric materials with complex structures such as Lead Zirconate Titanate (PZT) [5]. While EO thin films have garnered some success, the EO properties of these films still remain relatively low [6]. Despite the inherent limitations of thin films, novel device designs have allowed for progress to be made [7]. Continued research on thin film device design could allow for the production of competitive thin film EO devices [8].

Single crystal growth methods are equilibrium restricted techniques. This makes it difficult to grow complex EO materials in single crystal form. Bulk polycrystalline ceramic materials are not always restricted to this limitation. This can allow for the exploration of new EO systems. In particular, EO systems with complex structures can be pursued as this complexity could enhance the EO efficiency. While currently available EO devices are not made of toxic materials, many of the high performance materials being pursued are lead based. Exploration of EO polycrystalline ceramic materials will allow for additional flexibility in material selection so that toxic materials can be avoided.

1.3-Overview of Dissertation

In this work, a lead free polycrystalline ceramic will be introduced which has EO properties that outperform the materials used today. This material, a solid solution of barium titanate (BaTiO3), has a chemical formula of $(1\text{-}x)\mathrm{Ba}(\mathrm{Zr}_{0.2}\mathrm{Ti}_{0.8})\mathrm{O}_3$-$x(\mathrm{Ba}_{0.7}\mathrm{Ca}_{0.3})\mathrm{TiO}_3$ (BZT-BCT). In this work the material is referred to as BXT. It will be shown that BXT can be made transparent using a new powder synthesis technique in combination with an advanced processing method know as Current Activated Pressure Assisted Densification (CAPAD). These synthesis and processing procedures have a significant effect on the final sample quality. It will be shown that even small amounts of inhomogeneity in the densified ceramics can have an impact on the properties of BXT.

It will be shown that transparent BXT polycrystalline ceramics can be produced through optimization of the synthesis and processing conditions. The optical and EO properties of these transparent ceramics can then be explored. It will further be shown that BXT has extraordinary EO properties, surpassing even those of LN and the high performance lead based materials. The mechanism behind this excellent performance will be explored using additional EO and ferroelectric measurements. From these measurements it will be shown that BXT has a complex voltage induced structural transformation that enhances its EO properties.

Chapter 2-Background

2.1-Ferroelectric Phenomena

Although ferroelectricity is not always a requirement for EO phenomena (ex: GaAs), the most well studied and commonly applied EO materials are ferroelectrics. In these materials, the EO effect is deeply connected to the ferroelectric response of the material. It would therefore be prudent to examine ferroelectricity and its related phenomena in more detail.

Ferroelectricity is the property of some materials to sustain a spontaneous electrical polarization. While there are several varieties of ferroelectric material, each manifesting from different physical sources, this work will focus on the displacive ferroelectric variety. This phenomenon occurs due to a lack of centro-symmetry in the crystal structure. Perhaps the most well studied ferroelectric crystal structure (and the one most important to this work) is the perovskite structure, seen in Figure 2.1. The most simple perovskites follow the chemical formula ABO_3. Ferroelectricity occurs in the perovskite structure due to the offset center atom. This offset burdens the lattice with a permanent dipole moment.

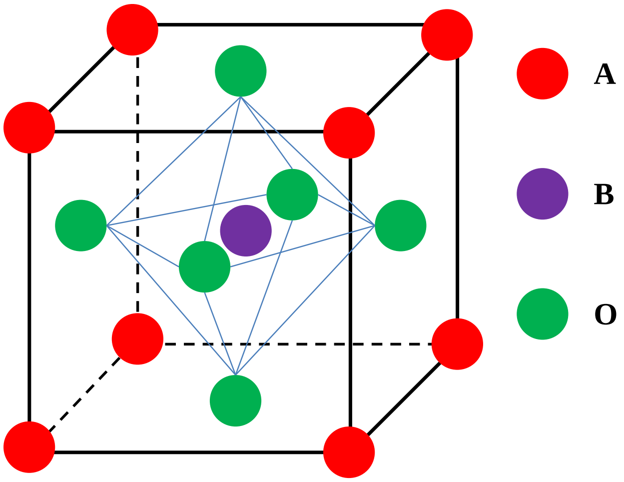

Figure 2.1: Schematic of the perovskite structure. In ferroelectric materials, the center atom (B) will be offset.

The presence of this dipole moment influences the unit cells nearby, causing them to form dipoles in similar directions. This local group of similarly oriented dipole moments is called a domain. Having all of the domains in a material pointing in the same direction would cause a permanent macroscopic charge, which is not energetically favorable. As a result, domains form in opposing directions to cancel each other out.

An interesting property of domains is that they change direction under applied field. Electric fields cause the local dipole moments to shift in the direction of the electric field. A simplified schematic of this can be seen in Figure 2.2. Domain motion and interaction play a critical role in all ferroelectric phenomena. For instance, domains cause the well-known polarization hysteresis loops found in ferroelectric materials. An example schematic of a ferroelectric hysteresis loop can be seen in Figure 2.3.

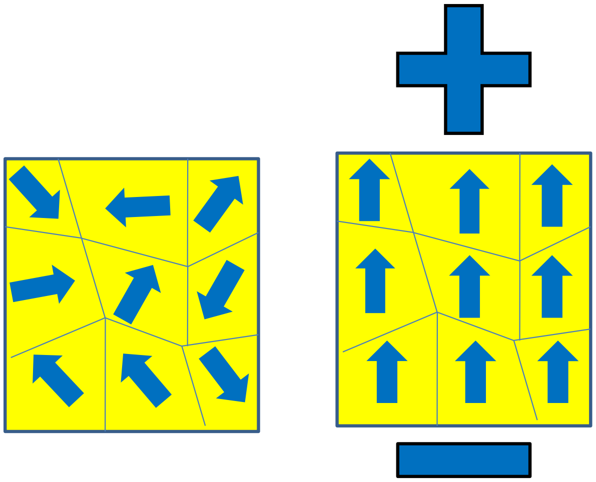

Figure 2.2: Simplified schematic of domains responding to applied electric field.

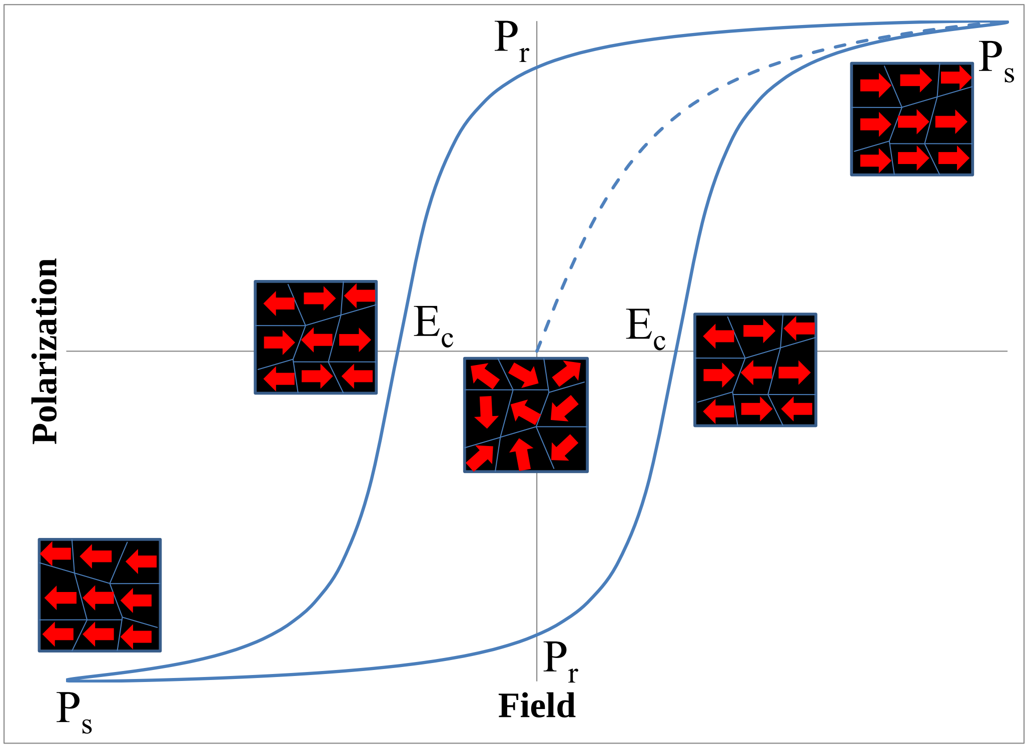

Figure 2.3: Example schematic of a ferroelectric hysteresis loop. The unpolarized initial curve is denoted with a dashed line.

The hysteresis loop allows for a few important ferroelectric properties to be discerned. The ferroelectric response begins in the center of the plot (indicating a discharged material with randomly oriented domains). When an electric field is applied to this material (in this example in the positive direction), the ferroelectric response follows a unique increasing polarization path (often called the initial/virgin curve). This occurs because the domains begin to align with the applied field, moving out of their random orientation. Continued application of electric field will cause the polarization to increase until a polarization limit is reached. This limit is called saturation, Ps, and occurs when the polarization mechanisms have been maximized and the domains are aligned.

Reducing the applied field causes the polarization response to decrease and the domains to flip. At zero field, the remanent polarization, P_r is reached. This is the spontaneous polarization that remains in the material, and is one of the key attributes of ferroelectric materials. At this point the domains are still partially aligned in the direction of the original applied field. If an electric field is applied in the opposite direction (in this case negative), the domains continue flipping until the coercive field, E_c is reached. The coercive field is the applied field necessary to produce zero net polarization and opposing domains. Continued increasing negative field causes the polarization to increase in the opposite direction until saturation. Reducing the applied field and then increasing in the opposite direction causes the previously mentioned events to occur again, closing the hysteresis loop.

Analysis of the hysteresis loop can provide a powerful insight into the underlying ferroelectric phenomena of the measured material. The saturation field of the material indicates the point at which the standard ferroelectric mechanisms have been exhausted. Typically, saturation indicates the point where the ferroelectric domains have found their final positions. Only dielectric phenomena will contribute to the polarization if the field is increased past this point. Saturation indirectly shows the highest practical operating field for that material.

Perhaps the most important ferroelectric parameter for practical applications is the coercive field. At the coercive field the domains directly cancel each other out, producing zero net polarization. Broadly speaking, the coercive field is the point where the polarization changes most rapidly with field. This can often be described as the point where domain motion becomes most efficient with respect to applied field. Other ferroelectric based properties often find their maximum value at the coercive field. This is also a strong impetus to pursue materials with low coercivities, as smaller coercivities often mean larger small-signal (low field) ferroelectric coefficients.

While the phenomena associated with ferroelectricity does not seem impactful at the microscopic scale, the cumulative effect of all these microscopic phenomena causes meaningful macroscopic property changes. When leveraged correctly, ferroelectricity can produce a meaningful change in almost every material property, generating an incredibly diverse array of sub phenomena. The most well-known of these sub phenomena is the piezoelectric effect. Ferroelectric materials under strain experience a distortion in the lattice. Due to the lack of centro-symmetry, this distortion cannot be compensated immediately, resulting in the generation of a charge.

Ferroelectric materials display many other well-known phenomena such as pyroelectricity and the photoelastic effect. Much like piezoelectricity, these phenomena originate as a side effect of the ferroelectric effect itself. A summary of the known ferroelectric phenomena can be seen in Table 2.1 (adapted from [9]). Ferroelectricity gives rise to a number of diverse and useful properties, the majority of which are already being used in a variety of industries. This is likely only a small sample of the properties that ferroelectric materials can display. It is highly likely that this table can be expanded greatly to include many other useful ferroelectric properties.

Table 2.1: Summary of ferreolectric phenomena.

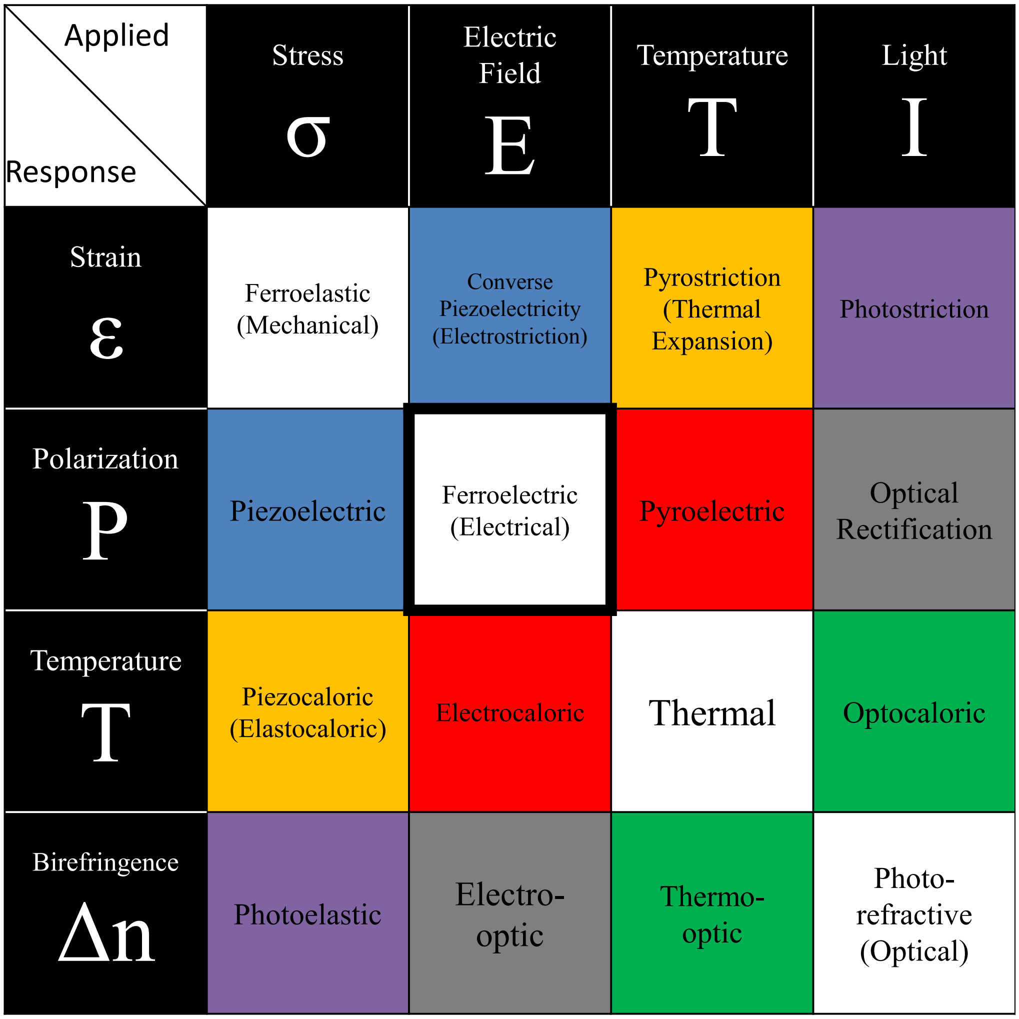

Applied Response	Stress σ	Electric Field E	Temperature T	Light I
Strain ε	Ferroelastic (Mechanical)	Converse Piezoelectricity (Electrostriction)	Pyrostriction (Thermal Expansion)	Photostriction
Polarization P	Piezoelectric	Ferroelectric (Electrical)	Pyroelectric	Optical Rectification
Temperature T	Piezocaloric (Elastocaloric)	Electrocaloric	Thermal	Optocaloric
Birefringence Δn	Photoelastic	Electro-optic	Thermo-optic	Photo-refractive (Optical)

2.1.1-Brief History of Ferroelectricity

The history of ferroelectricity actually does not begin with ferroelectricity itself. It begins with the formal discovery of pyroelectricity by the father of modern experimental optics, David Brewster, in 1824 [10]. Piezoelectricity was then discovered in 1880 by Pierre Curie and Jacques Curie [11]. Finally, in 1921 ferroelectricity was discovered in Rochelle Salt by Joseph Valasek [12]. This was an impressive feat for the time, considering the lack of modern electronics, thus earning him the moniker “The Father of Ferroelectricity”.

Until the outbreak of World War II, research on ferroelectric materials primarily involved single crystals and minerals. The war prompted intense research into high dielectric constant capacitors for use in electronics. A major breakthrough came from the discovery of polycrystalline BaTiO3 (BT) by Hans Thurnauer and James Deaderick from the American Lava Corporation in 1941 (although the patent was not disclosed until 1947) [13]. The ferroelectric nature of BT was not discovered until 1947 when one of the Fathers of Modern Materials Science, Arthur Von Hippel, published his landmark work on high dielectric constant ceramics [14]. This discovery led to an explosion of work in the field of ferroelectric and piezoelectric ceramics, paving the way for our modern understanding of these materials.

2.2-The Electro-Optic Effect

2.2.1-Electro-Optic Phenomena

The linear EO effect was discovered independently in 1883 by Wilhelm Röntgen [15] (the discoverer of X-Rays) and August Kundt [16] (known for measuring the speed of sound in gases and solids). The linear EO effect was not truly understood until Friedrich Pockels published his landmark paper on the subject in 1893 [17]. This intimidating 200 page article meticulously described experimental and mathematical evidence of the EO effect in a variety of piezoelectric crystals. For this reason the linear EO effect is commonly called the Pockels effect. It is interesting to note that the mathematical rigor that Pockels displayed in his work on EO and photoelastic phenomena came from the influence of his Ph.D advisor, Woldemar Voigt (who created the concept of a tensor).

Stated most simply, the electro optic effect is a material phenomenon where the optical properties of the material change when that material is exposed to an electric field. While there are many EO materials that are not ferroelectric, this work will deal exclusively with EO materials that are also ferroelectric. In these kinds of EO materials there is a change in index of refraction *n* with applied field. This effect can occur due to a variety of reasons.

The most simple expression of the linear EO effect is when the applied electric field distorts the electronic environment in a material due to shifting ion and electron positions. In a material that lacks centrosymmetry (ferroelectrics) this electronic distortion is not compensated evenly, and a change in the optical property results. This effect will dominate in simple EO materials such as single domain single crystals. These phenomena often dominate the EO effect at very high (GHz) frequencies as well.

Domain physics plays a critical role in most ferroelectric phenomena, so it would be understandable that it would play a role in EO properties as well. A ferroelectric domain contains a homogenous collection of crystal anisotropy. In most non ferroelectric birefringent ceramics, the individual grains themselves are the smallest unit of crystallographic alignment. In ferroelectric materials, domains further subdivide the ceramic into even smaller units of alignment. Much like grains the domains overall represent a random orientation of optical axes contributing to the effective index of refraction, $\bar{n}$, of the ceramic.

Ferroelectric domains change dramatically in response to applied electric field. Domains can move, rotate their orientation, combine with other domains, and subdivide into even smaller domains. Such activity has a considerable impact on the local index of refraction and birefringence state, leading to a change in $\bar{n}$. Although the individual changes in the domain state are small, the cumulative effect through the whole ceramic results in a meaningful modification of the optical properties [18].

All ferroelectric materials are inherently piezoelectric. The application of an electric field will activate the piezoelectric effect and cause the dimensions of the ceramic to change. These dimension changes will occur during the application of the EO effect as well. This will result in a change in the amount of material that the modulated light is exposed to, changing the birefringence state of the ceramic. Significant amounts of strain in the lattice can also contribute to the EO effect through the photoelastic effect.

Most ferroelectric based EO materials will experience all three of these phenomena. A schematic summarizing this can be seen in Figure 2.4 (ionic effects are implied). Electric field induced phase or structural transitions can also contribute to the EO effect. While not common in displacive ferroelectrics, these transitions are often the reason for the strong EO effect found in relaxor ferroelectric materials.

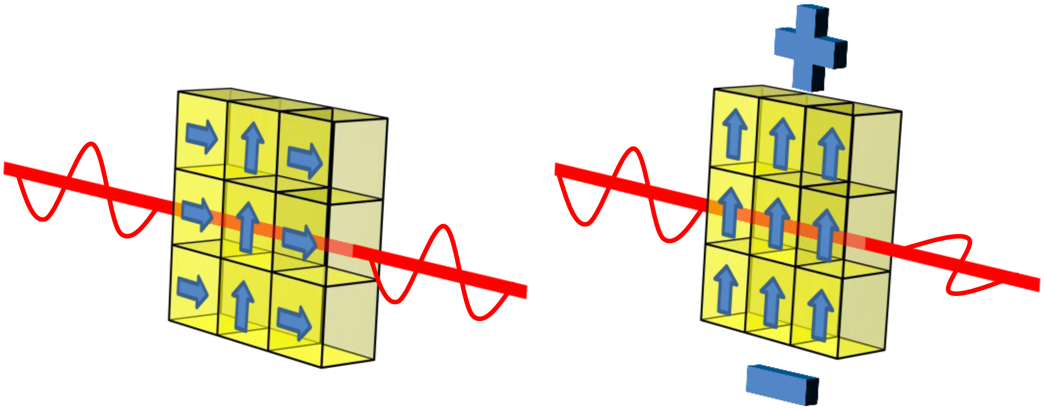

Figure 2.4: Schematic showing common elements that influence the EO effect in displacive ferroelectrics (ionic/electronic contributions are not shown).

2.2.2-The Electro-Optic Effect in Practice

For standard displacive ferroelectric materials, the EO effect is linear and is governed by the equation:

$$\Delta n = \frac{1}{2} n_0^3 r E \qquad 1$$

where n_0 is the refractive index without field, E is the applied electric field, and r is the EO coefficient. This change in index of refraction can be used directly to modify the phase of the light. Changing the phase of input light is the most simple of EO applications, requiring no additional optical components.

Under the proper conditions, this effect can be used to adjust the EO materials birefringence. Birefringence occurs when the two components of light are exposed to two different electronic conditions (indices of refraction). This produces a relative phase change between the two components of light, modifying the ellipticity and angle of the polarization. A static waveplate will follow the standard equation for relative phase change Γ due to birefringence:

$$\Gamma = \frac{2\pi}{\lambda} L\Delta \mathrm{n} \qquad 2$$

where λ is the wavelength of light and L is the material length that the light travels through.

The condition that causes a change in the polarization condition of the input light can be seen in Figure 2.5. Linearly polarized light oriented 45° from the direction of the applied field will be exposed to a voltage dependent birefringence state. Such an orientation exposes one component of light to the field axis while the other component of light is exposed to the perpendicular axis. An applied electric field will produce an EO effect, causing an unequal distortion in the electronic environment that both components of light experience (effectively producing a birefringence). The reliance on both axes gives this phenomenon its name, the composite EO effect (sometimes called compound or combined EO effect). This causes the linearly polarized light to become elliptical and rotate angle, effectively making EO materials voltage controllable waveplates.

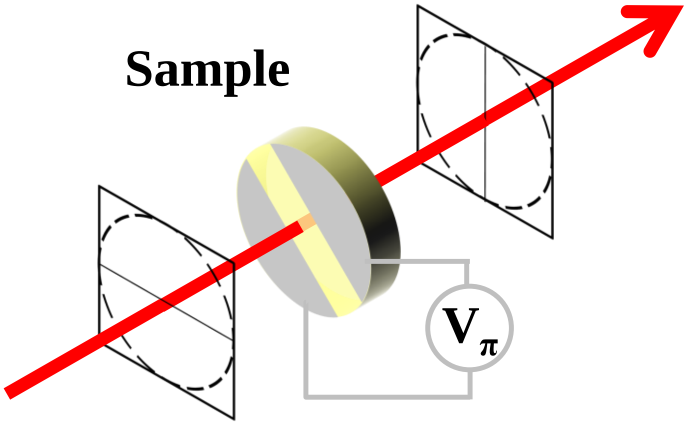

Figure 2.5: Schematic of a condition that leverages the EO effect. Under applied field the EO material will rotate the polarization of light.

The desired end state for this kind of EO application is when the birefringence is modified to the point that the polarization is returned to its linear state and rotated by 90°. This scenario constitutes one of the primary uses for EO materials. An EO material placed between two crossed linear polarizers can be used to modulate incident light with an applied voltage. In standard displacive ferroelectrics, this scenario is controlled by the composite EO coefficient r_c. The governing equation can be derived by combining equation 1 and equation 2 and setting $\Gamma = \pi$ (a full 180° phase shift producing a polarization change of 90°) to make:

$$r_c = \frac{\lambda}{V_\pi n_0^3}\left(\frac{d}{L}\right) \qquad 3$$

where d is the spacing between electrodes and V_π is the half wave voltage. V_π is the voltage required to produce a full 180° phase rotation, completely modulating the EO material. In the case of two crossed polarizers, an application of V_π would cause the output light signal to modulate from 0% to 100% intensity.

2.3-Optical Transparency in Polycrystalline Ceramics

One of the advantages of optical single crystals is their high transparency. Single crystals commonly lack scattering and absorption sites. This allows light to travel through single crystals undisturbed, even with very thick crystals. Polycrystalline materials, being a composite of individual crystallites, provide a lot of opportunities to scatter light. A highly optimized microstructure is required to produce transparent polycrystalline ceramics. The three most common sources of scattering in polycrystalline materials are shown schematically in Figure 2.6.

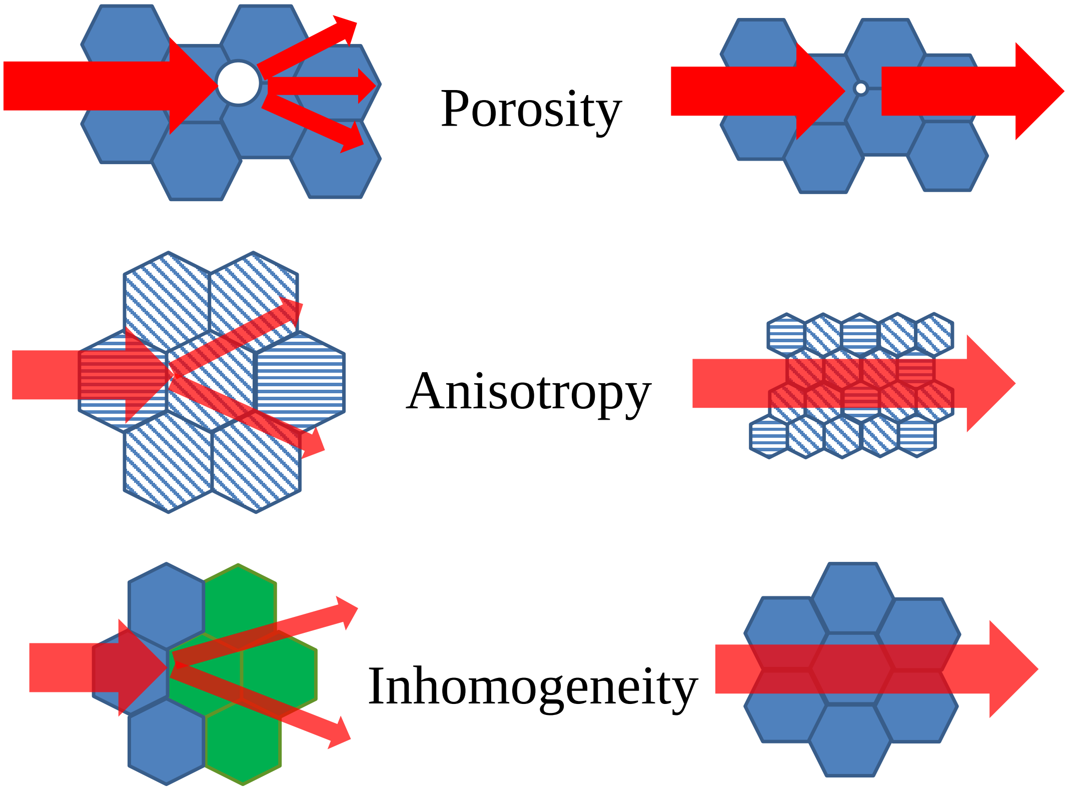

Figure 2.6: Schematic representation of the most common sources of light scattering in polycrystalline materials.

Porosity is perhaps the most efficient light scattering defect, due to the large difference in index of refraction between the material and the pore. Even small amounts of residual porosity can render a ceramic completely opaque. Scattering at grain boundaries can occur in optically anisotropic materials due to the difference in refractive index between the randomly oriented grains. The inherent structural asymmetry found in ferroelectric materials makes them sensitive to this source of scattering. Finally, scattering can occur due to the presence of inhomogeneities in materials that are not fully reacted. Material systems that rely on complex synthesis or reaction methods will be sensitive to this form of scattering.

It can be difficult to identify the sources of scattering in densified ceramics since there will be contributions from all three factors. One method of qualitatively assessing the origin of the scattering is by fitting the dispersion of the effective optical loss, α_{eff} to known models. Since the optical loss contains both scattering and absorption information, one must assume that absorption does not vary with wavelength to do this analysis. One such model is the Mie solution of Maxwell's equations. Approximations of the Mie solution can be used for obtaining some insight into a ceramics scattering processes [19]. One example is the Rayleigh approximation, which is valid if there is a large difference in refractive index between the scattering site and the matrix (i.e. porosity). Optical loss will be proportional to $1/\lambda^4$ in this case. Another example is the Rayleigh-Gans-Debye (RGD) approximation, which is valid for small differences in refractive index (i.e. anisotropy). In this case optical loss will follow a $1/\lambda^2$ law. Examining the linearity of α_{eff} under both conditions will indicate what scattering mechanisms are active.

The previously mentioned sources of scattering can be overcome through careful optimization of microstructure. Scattering from porosity can be minimized by eliminating or shrinking the pores themselves. Only highly dense ceramics can achieve transparency. Scattering at grain boundaries can be minimized by reducing the grain size of the polycrystalline ceramic. Grains smaller than the desired wavelength of light do not significantly interact with that light. Finally, ensuring a fully reacted and homogeneous microstructure will prevent scattering from inhomogeneities. This may require pursuing more efficient synthesis methods or paying careful attention to the level of homogeneity in the material.

2.4-Ferroelectric Materials

2.4.1-Lead Based Ferroelectric Materials

It is impossible to discuss ferroelectric materials without first discussing the pervasiveness of lead based ferroelectric devices in modern electronics. Lead Zirconate Titanate (PZT) in particular, is nearly ubiquitous in current piezoelectric devices. The excellent piezoelectric properties of PZT come from its unique phase condition. PZT containing a Zr:Ti ratio of 52:48 falls on what is called the Morphotropic Phase Boundary (MPB), a boundary between two ferroelectric phases (Rhombohedral and Tetragonal in the case of PZT)[20]. When on this phase boundary, PZT has access to two ferroelectric phases, giving PZT more flexibility for domain motion and vastly improved ferroelectric properties.

Although PZT was originally discovered in Japan [21], it was not until 1954 that the piezoelectric properties of PZT at the MPB were discovered by Bernard Jaffe [22]. This began a rush of research on the PZT system. While the MPB provides PZT with an innate advantage over other piezoelectric materials, PZT also has over half a century of research and optimization. By the time lead toxicity had become widely known and accepted, PZT was already entrenched in the world of modern electronics. A lack of desirable alternatives to PZT has stimulated several generations of scientists to pursue the field of high performance lead free piezoelectric materials.

Despite its toxicity, PZT is still widely studied as a model piezoelectric system. Major discoveries with applications to all ferroelectric phenomena are still being produced because of research into PZT. In 1999 the Father of Modern Ferroelectricity, Eric Cross, discovered that PZT has a monoclinic phase between the Rhombohedral and Tetragonal phases at the MPB [23]. While there is still debate about the origins of the large piezoelectric effect in PZT, it is generally believed that the MPB, the monoclinic phase, and the presence of nano domains all play a role [24].

2.4.2-Electro Optic Materials

As stated previously, modern EO devices rely heavily on LN. While LN is very stable, it has a relatively low EO coefficient of r_c = 20 pm/V [25]. This is due to LN relying on simple ferroelectric mechanisms to provide its EO effect (mostly ionic/electronic contributions [26]). Ferroelectric materials with additional mechanisms should have a high EO coefficient. Unfortunately, material systems with complex phase or structural conditions are difficult to grow in single crystal form.

Lead lanthanum zirconate titanate (PLZT) was the first reported EO polycrystalline ceramic. It was discovered in 1971 by Gene Haertling and Cecil Land from Sandia National Laboratories [27]. This landmark work earned Gene Haertling the moniker “The Father of PLZT” and created the field of EO ceramics [28]. Haertling was able to produce transparent PLZT using hot pressing. Many compositions of PLZT had exceptional EO properties as well. Despite being a considerable scientific achievement, the high lead content of these materials provides an ecological and health concern. This has created an opportunity for a lead free EO ceramic to be developed.

2.4.3-Barium Zirconate Titanate Barium Calcium Titanate

Despite the efforts of the piezoelectric community, PZT has remained the dominate piezoelectric system for the past several decades [20]. This is largely due to the fact that a viable lead free alternative to PZT had not been invented. This changed in 2009 when Wenfeng Liu and Xiaobing Ren developed a new lead free piezoelectric that has properties that are comparable to or better than PZT [29]. The material they discovered was $(1\text{-}x)Ba(Zr_{0.2}Ti_{0.8})O_3\text{-}x(Ba_{0.7}Ca_{0.3})TiO_3$ (BZT-BCT or BXT in this work). Aside from its excellent piezoelectric properties, BXT has properties that make it competitive in many other applications such as high energy density capacitors [30] and pyroelectric sensors [31].

The mechanisms behind the exceptional piezoelectric properties in BXT are still under investigation. Much like PZT, BXT has a complex structural state owing to the fact that the $x = 50$ composition lies on a phase boundary. This phase boundary separates a rhombohedral and a tetragonal perovskite phase. It was originally proposed that the piezoelectric properties of BXT are due to the presence of a MPB [29] [32]. Also like PZT, it was recently discovered that BXT has an intermediate phase between the tetragonal and rhombohedral phases. For BXT this intermediate phase is orthorhombic [33]. There is even some speculation that a monoclinic phase exists in BXT, although careful rietveld refinement indicates that this unlikely [34]. While the exact reasons for the exceptional properties in BXT are still being investigated, it is likely that they are related to this orthorhombic phase [35].

A summary of the crystal structures potentially available to BXT can be seen in Table 2.2. At room temperature, the $x = 50$ composition should only have access to the orthorhombic and tetragonal phases. At the curie temperature (~93 °C) BXT enters its paraelectric cubic phase. It is important to note that BXT has access to a wide array of optical symmetries. Conservatively, BXT can have access to one uniaxial and one biaxial phase at room temperature. Liberally, BXT could have access to many other phases with unique optical traits. The phases BXT can have will have a profound impact on its optical and EO properties

Table 2.2: Summary of the possible crystal structures potentially available to BXT.

Structure	**Space Group**	**Optical Symmetry**
Cubic	$Pm\bar{3}m$	Isotropic
Tetragonal	P4mm	Uniaxial
Rhombohedral	R3m	Uniaxial
Orthorhombic	Am22	Biaxial
Monoclinic	Pm	Biaxial

The work by Liu and Ren was not first to be done on BXT. The $(Ba,Ca)(Ti,Zr)O_3$ system was originally examined in 1954 [36], although the properties of the system were not explored. Since then the non MPB stoichiometry’s of this system, called BCZT at the time, were explored in thin film [37] and bulk form [38] for its dielectric properties. The discovery of the MPB properties of BXT has ignited major interest in this material system. The citations per year for the original Liu and Ren article (according to Google Scholar) can be seen in Figure 2.7. As of the writing of this work, the article has been cited 893 times. The upward trajectory of the citation rate indicates that BXT has a very promising future as a lead free piezoelectric material. BXT has already found its way into ultrasound medical devices [39].

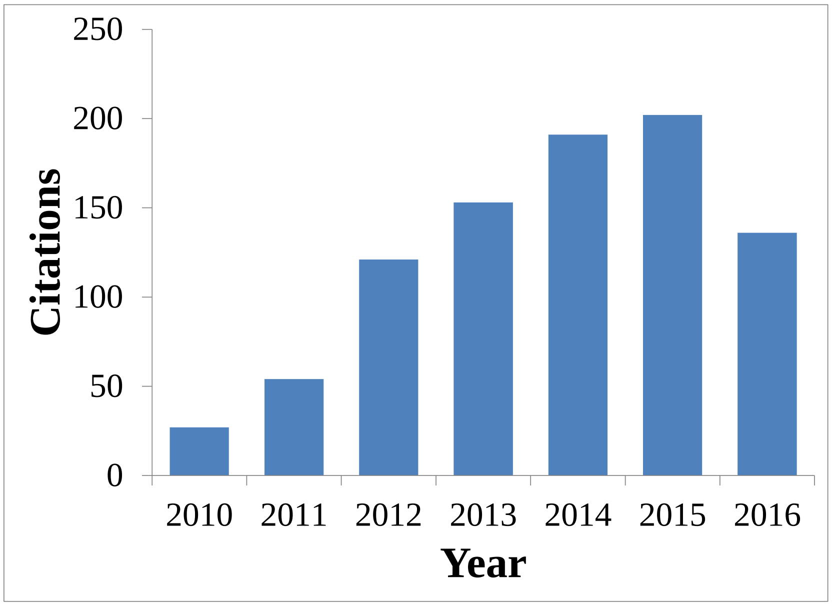

Figure 2.7: Bar graph showing the Google Scholar citation data by year for the original BZT-BCT article by Liu and Ren.

2.5-Current Activated Pressure Assisted Densification (CAPAD)

2.5.1-Conventional Materials Processing

As stated earlier, microstructural condition will strongly influence the optical properties of polycrystalline ceramics. It is necessary to process optical ceramics using a densification technique that allows sufficient microstructural control to produce the desired optical properties. Conventional densification methods, such as free sintering, have difficulty producing samples with a high enough density to allow for optical transparency. Free sintered materials often suffer from trapped porosity due to the slow heating rates involved. The addition of applied pressure, such as in hot pressing, provides another driving force for sintering. True microstructural optimization, however, can only be achieved with complete control over the processing conditions.

This is not to say that optical materials cannot be processed using conventional techniques. The most famous example is of transparent alumina made by Robert Coble [40]. Coble was able to make alumina transparent with conventional sintering by doping it with MgO. This pinned the grain boundaries during densification, preventing grain growth and avoiding trapped porosity. Although this was a monumental discovery (cementing Coble as one of the most important materials scientists of his generation), such a processing method is indicative of the mindset involved in traditional ceramics processing.

The idea of traditional ceramics processing is one of compromise. Often, one or two microstructural components are sacrificed to optimize the remaining components. This sacrifice can be commonly seen when researchers use nanocrystalline powder to enhance densification in free sintered ceramics. The starting nanocrystallinity is sacrificed to achieve high density in the final product. Microstructural sacrifices can be seen on the industrial scale with sintering using liquid phases or sintering aids. An undesirable addition is added to the ceramic to enhance densification, sacrificing the purity of the material to achieve a higher density. A diagram of the microstructural components and some common penalties associated with their sacrifice can be seen in Figure 2.8. While bartering microstructural components has worked well in producing the foundation of the ceramics that are in use today, the materials of the future will need to be made without microstructural compromises.

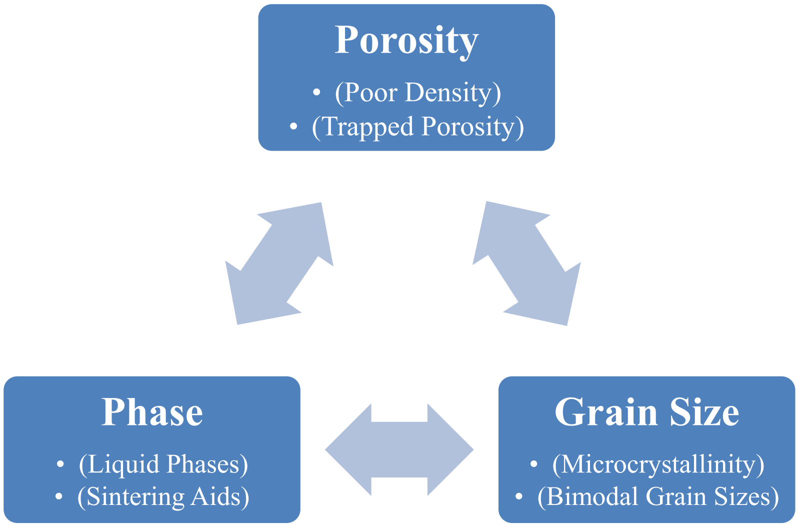

Figure 2.8: A schematic of the microstructural features in ceramics. Penalties associated with forgoing control over the associated feature are listed below it.

2.5.2-Introduction to CAPAD

Current Activated Pressure Assisted Densification (CAPAD), commonly known as Spark Plasma Sintering (SPS), has emerged as one of the most promising powder consolidation methods in recent history. This materials processing method involves the use of large electric currents and high pressures to densify materials more quickly and at lower temperatures than conventional sintering [41]. A considerable number of materials have already been processed using the CAPAD technique [42]. This process is particularly exceptional at producing nanocrystalline ceramics [43]. Fully dense materials with grain sizes less than 20nm are even possible using this technique [44]. The CAPAD technique is uniquely qualified for processing EO BXT because it has already been used extensively in processing piezoelectric materials [45] as well as optical materials [46].

A basic schematic of a CAPAD device can be seen in Figure 2.9. CAPAD operates by passing a large electric current through a die and plunger assembly containing the sample to be densified. The temperature of the die and plunger assembly increases due to joule heating. This method heats the sample directly, allowing for very rapid heating rates. Additionally, pressure is applied to the die and plunger assembly through the electrodes. Pressure will have an enormous impact on densification rates produced during CAPAD processing [47]. The presence of current will also often generate a non-negligible impact on the reactivity and densification of systems processed using CAPAD [48]. Fast heating, high pressures, and the potential for current based effects allow CAPAD to produce high density ceramics with controlled microstructures. This makes the CAPAD technique ideal for densifying viable EO ceramics.

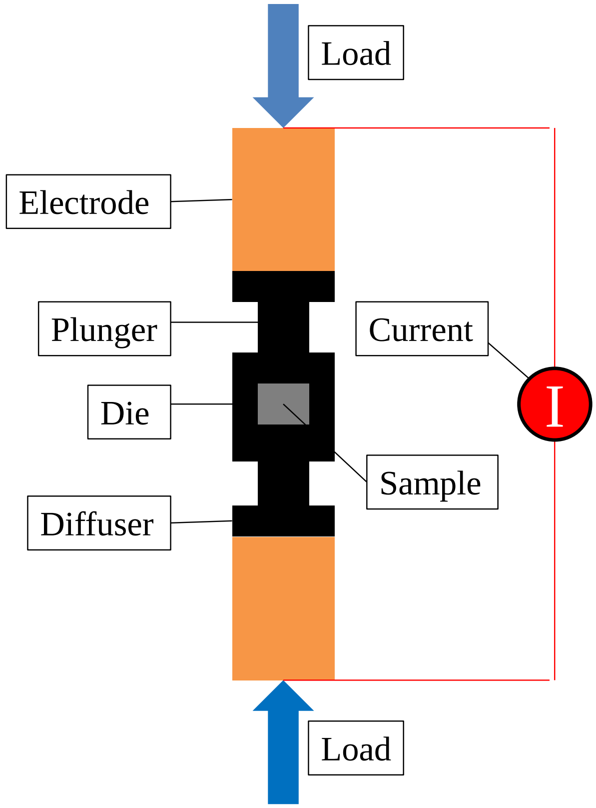

Figure 2.9: Simplified schematic of a CAPAD device and its operation.

Many of the microstructures required for optical transparency are not stable against high temperature and long processing times. CAPAD allows for materials to be processed at lower temperatures. This can be used to avoid high temperature events that might be detrimental to the material being processed, such as dissociations and unwanted phase changes. The rapid heating and cooling rate of the CAPAD process allows for metastable microstructures to be maintained. Nanocrystallinity in densified ceramics is often not stable against high temperatures and long processing times. CAPAD is exceptional at producing nanostructured ceramics because the ceramics are not exposed to the conditions that produce microstructural equilibrium for long enough. It has even been demonstrated recently that CAPAD can be used to defeat solubility limitations in doped material, such as rare earth doped alumina [49].

Chapter 3-Experimental Procedures

3.1-Processing

All samples densified during this study were processed using a custom built CAPAD device made at the University of California, Riverside. The processing occurs in a stainless steel water cooled high vacuum chamber (MDC Corp. Hayward, CA). A vacuum of <5x10-2 torr is provided by an Alcatel direct drive rotary vane vacuum pump (adixen Vacuum Products, Annecy, France). Currents up to 6000A were produced using a Silicon-Controlled Rectifier (SCR) DC power supply (Benjamin Power Group, Northbrook, Il). Load is applied using an Instron 5584 Universal Test Frame (Instron Inc, Norwood, MA). Temperature is acquired using an ungrounded N-Type thermocouple (Omega Engineering Inc, Stamford, CT) or an optical pyrometer (Chino, Tokyo, Japan).

A list of CAPAD operating parameters used in this study is outlined in Table 3.1. Parameters with ranges will be discussed in more detail in their corresponding chapters. All samples were prepressed at 70 MPa for 1 minute before densification. After CAPAD densification was finished the load was gradually removed while the samples were cooled at 50 °C/min.

Table 3.1: Outline of CAPAD parameters used in this study.

Parameter	**Value**
Temperature (°C)	1000-1300
Max Pressure (MPa)	100
Heating Rate (°C/min)	25-200
Load Rate (MPa/min)	35
Temperature Hold (min)	5-10
Cooling Rate (°C/min)	50

3.2-Ferroelectric Hysteresis Measurements

At its core, ferroelectric phenomena and ferroelectricity itself are the result of a polarization that varies nonlinearly and hystereticaly with applied field. This polarization response manifests itself as a nonlinear current draw under applied fields. This allows for the polarization response of a ferroelectric material to be conveniently measured by analyzing the current during applied field. Due to the highly insulating nature of most ferroelectric materials, a standard ampmeter cannot be used. Although not very common, a high precision current measuring device (such as a picoammeter) can be used for ferroelectric measurements.

Ferroelectric properties are more commonly measured using a Sawyer-Tower circuit. This technique was discovered in 1930 by Charles Sawyer and Charles Tower [50]. A circuit diagram of this technique is shown in Figure 3.1. This circuit design takes advantage of the fact that capacitors in series draw the same current. Using this principle, the polarization *P* generated in the sample can be determined by:

$$P = \frac{V_R C_R}{A} \qquad 4$$

where V_R is the voltage measured across the reference capacitor, C_R is the capacitance of the reference capacitor, and A is the area of the sample.

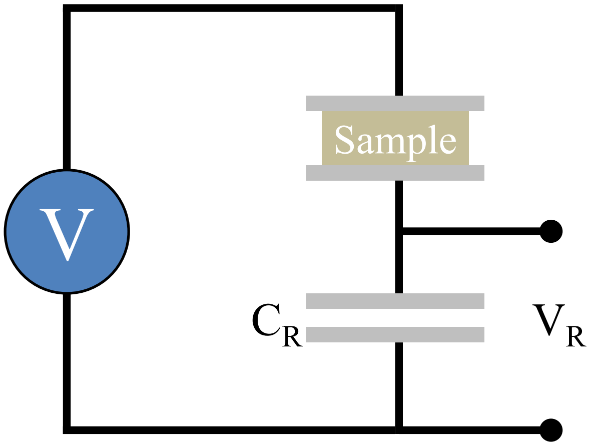

Figure 3.1: Schematic of the original Sawyer-Tower circuit used for measuring ferroelectric polarization.

A more modern Sawyer Tower circuit can be seen in Figure 3.2. This design makes use of an op-amp (in an integrator configuration) to provide a virtual ground for the Sawyer Tower measurement. The virtual ground design reduces the voltage losses by forcing the system to have a stable ground. Another advantage of the virtual ground technique is that the measurement is performed in the same way as a standard Sawyer Tower measurement, including using equation 4.

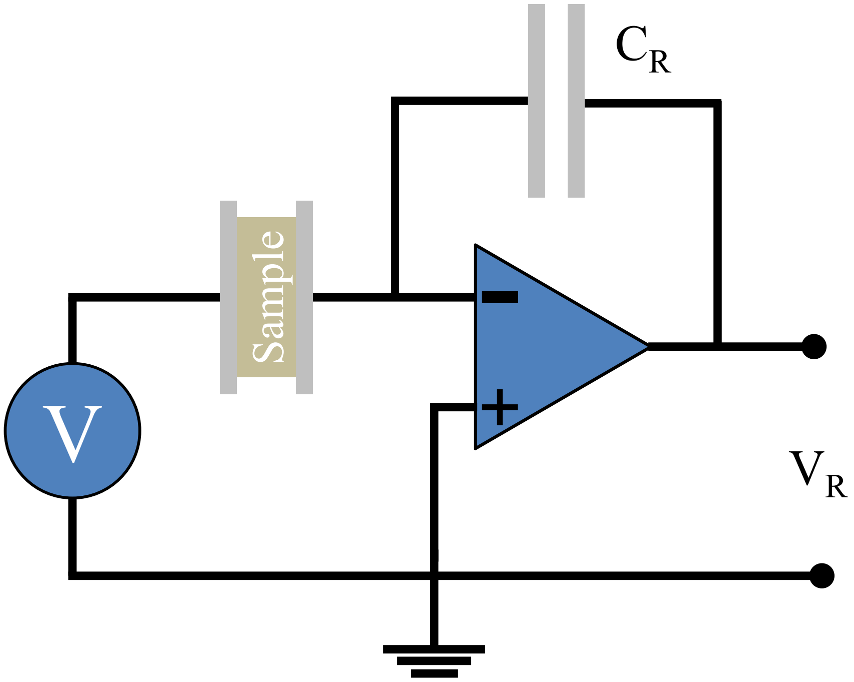

Figure 3.2: Schematic of a virtual ground sawyer-tower circuit.

For the purposes of this study, a custom virtual ground Sawyer Tower circuit was built. Measurements were performed using a Trek 610E high voltage power supply (Trek Inc, New York, USA) being modulated by a Rigol DG4062 function generator (Rigol Technologies Inc, Beijing, China). Silver paste was applied to the faces of the samples so they could be measured in a parallel plate capacitor orientation. All measurements were performed at room temperature and in oil to avoid arcing. Measurements were performed on commercial PZT-850 ceramics (American Piezo Ceramic, Ltd., Mackeyville, PA) to determine the validity of the system.

3.3-Electro-Optic Measurements

3.3.1-Measurement Methods

As stated previously, the EO effect can be used to modify light by changing the phase or the polarization state. Both of these changes can be measured directly to determine the efficiency of the EO material. A change in phase can be measured using an interferometer. By placing the EO material along one leg of the interferometer, one can determine the phase change by examining the interference when the two beams are recombined. This technique is useful for determining the individual tensor components of the EO effect. The lack of discernable macroscopic tensoral effects in polycrystalline materials makes this technique unsuitable for measuring the EO effect in ceramics.

Since the compound EO effect results in a change in the polarization of light, a measurement technique that examines the rotation of polarization would allow for the direct determination of r_c**.** One such device is a Senarmont compensator, invented by Henri Senarmont in 1840 [51]. This device commonly uses crossed polarizing filters to produce a null state. Placing a sample between the crossed polarizers allows for the rotation of polarization to be monitored. This can be done by orientating the electric field direction 45° away from the polarization axis, allowing the compound EO effect to be leveraged. A simplified schematic of a senarmont compensator used as an EO measurement device can be seen in Figure 3.3. As an electric field is applied to the sample being measured, the relative intensity of light exiting the final polarizer (referred to as the analyzer) increases from 0% to 100%. The voltage required to change the relative intensity from 0% to 100% is the V_π. The EO coefficient can then be calculated using equation 3.

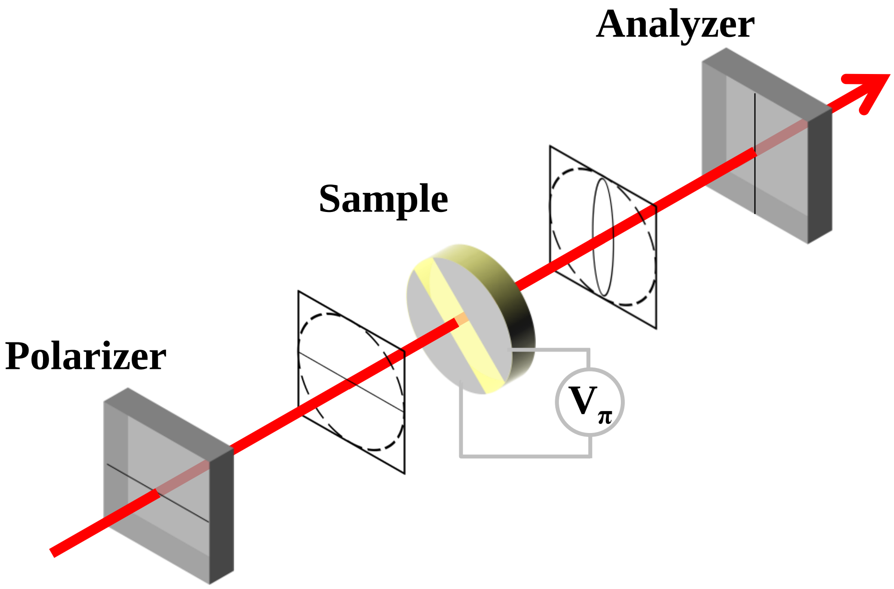

Figure 3.3: Schematic of a senarmont compensator used for measuring the EO effect.

3.3.2-Custom Built EO System

For the purposes of this study, a custom built elipsometric (one beam) amplitude modulator in a modified Senarmont Compensator style was constructed. The voltage was delivered using a Trek 610e high voltage power supply driven by a Rigol DG4062 function generator. Silver electrodes were applied to the samples in a transverse style with a 2 mm gap between electrodes. Light was detected using a DET36A photodetector (Thor Labs, New Jersey, USA). A red diode laser (λ = 635 nm) was used for all EO measurements. A photograph of this system can be seen in Figure 3.4. For this study, a single crystal of Z-cut $LiNbO_3$ was used as a reference standard.

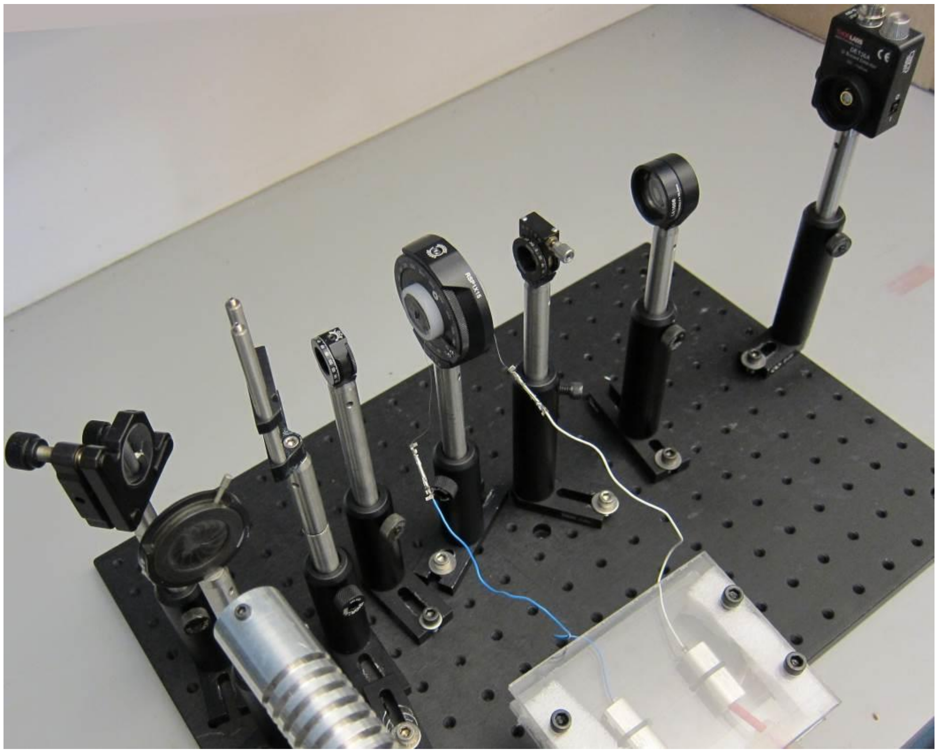

Figure 3.4: Photograph of the custom built senarmont compensator used in this study.

3.3.3-Bias Field measurements

One of the challenges associated with the study of ferroelectric materials is that it can be difficult to determine the exact mechanisms that contribute to the ferroelectric effect. This is particularly true in materials like PZT and BXT which have complex phase and domain activity interacting and influencing the ferroelectric phenomena. One common method of exploring ferroelectric mechanisms is by performing "large signal" coefficient measurements. Most ferroelectric coefficients reported in literature are small signal coefficients. This means the coefficients are measured at the smallest field possible to produce a meaningful effect. Values such as d_{33} (piezoelectric coupling coefficient), ε

(relative permittivity), and r_c are small signal coefficients. These coefficients are ubiquitous because of their technological importance and practicality.

Large signal coefficients are ferroelectric properties measured at electric fields greater than is necessary for normal operation. These large signal measurements are useful because ferroelectric mechanisms are often exaggerated at high electric field. Fields in excess of certain values can also activate or deactivate certain mechanisms. High field measurements can provide valuable insight into the active ferroelectric mechanisms in the material, especially when the various large signal measurements are used in conjunction with one another.

In this work, large signal EO properties are determined using the bias field method. This method relies on finding local values of V_π at high electric fields. These measurements can be done in a senarmont compensator by monitoring the output intensity of light while the sample is subjected to a DC electric field. An example schematic of the expected signal (for a simple EO material) can be seen in Figure 3.5. As the polarization of light is rotated, the output intensity will oscillate between 0 and 100%. The bias voltage is the voltage between the local maximum and minimum while the voltage difference between the local maxima and local minima is the corresponding V_π. Using equation 3, the bias field r_c values can be calculated.

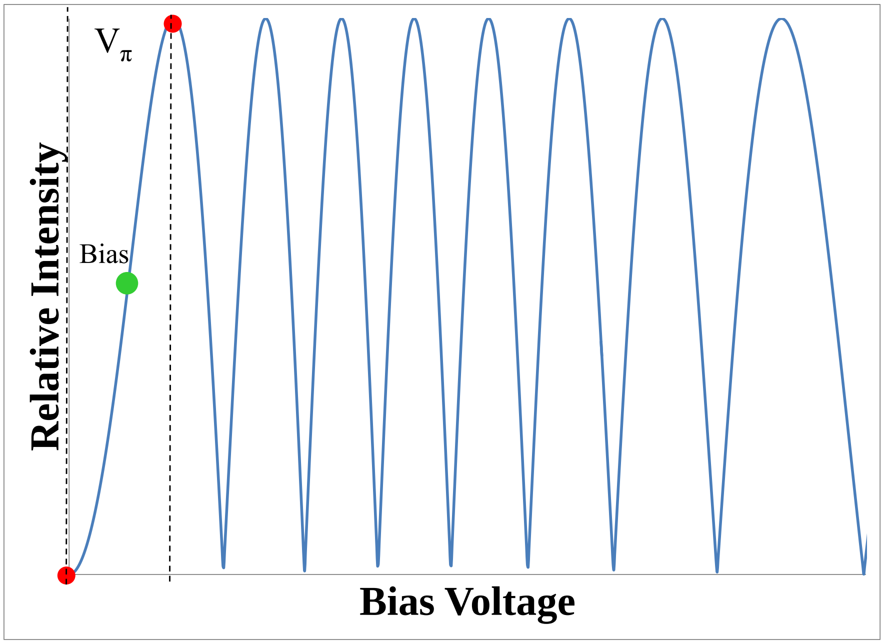

Figure 3.5: Schematic data of relative light intensity vs bias voltage during an EO bias field measurement for a simple EO material.

In Figure 3.5 it is important to note that the period between the intensity waves is not constant. Therefore, V_π and r_c will change considerably with bias voltage. An example schematic of an EO bias field measurement can be seen in Figure 3.6. This schematic represents what would be expected from a standard displacive ferroelectric material, such as $BaTiO_3$ [52]. As the bias field is increased, the EO coefficient will commonly increase due to increasing domain activity. This reaches a maximum at the coercive field, E_c. After this the EO effect will decrease due to the saturation of the available mechanisms. The value of r_c does not go to zero due to the contribution of the quadratic EO effect, which is most active at high electric fields.

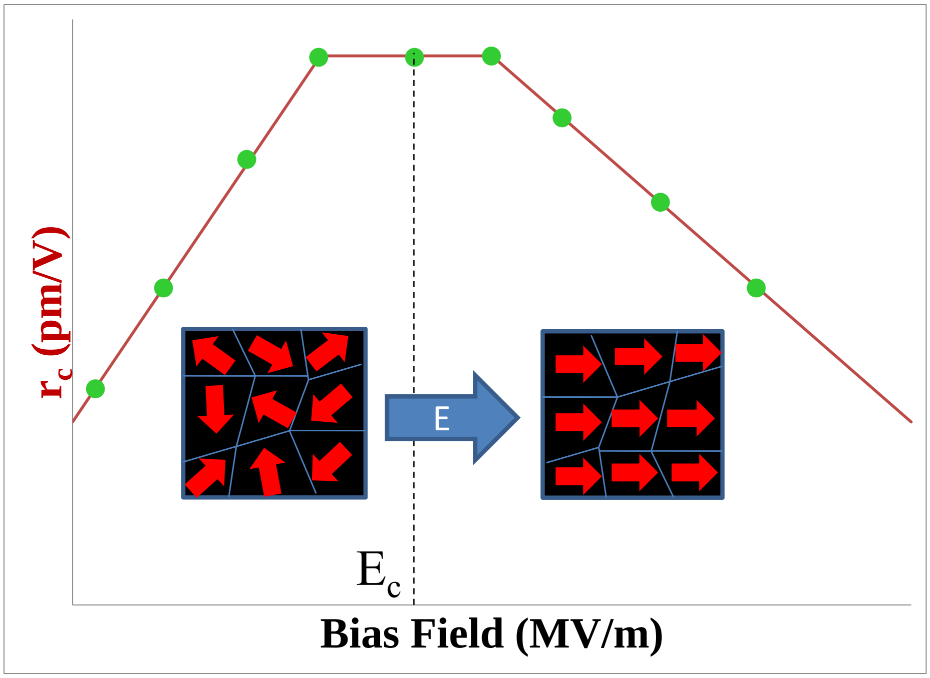

Figure 3.6: Expected schematic data of EO coefficient vs bias field during an EO bias field measurement for a simple EO material.

Chapter 4-Influence of Synthesis on Reaction in BXT

4.1-Introduction

BXT powders are most commonly synthesized using a solid state method. This synthesis method uses a powder mixture consisting of $BaCO_3$ (56.37 wt%), $BaZrO_3$ (10.53 wt%), $CaCO_3$ (5.72 wt%), and TiO_2 (27.38 wt%) [29]. The primary component by weight for this mixture is $BaCO_3$ (BC). These components are mixed and then calcined at high temperature (typically 1300°C). Powders synthesized this way have produced piezoelectric BXT ceramics with excellent properties. Unfortunately the high calcining temperatures used in this technique result in large grains and heavy agglomeration, restricting the potential for microstructural optimization.

A high calcining temperature is required for BC based mixtures because they are based on traditional methods of making $BaTiO_3$ (BT). BT is commonly synthesized using BC and TiO_2. High calcining temperatures (1250-1300 °C) are needed to completely decompose BC and ultimately form BT [53]. The reaction temperature for BT can be reduced by using finer starting powders [54]. Unfortunately the complete decomposition of BC is always required to form BT, which will limit the minimum temperature needed using this method.

Some work has been done on producing BXT powders using methods other than solid state synthesis, such as sol gel [55][56] and auto combustion methods [57]. These methods resulted in nanocrystalline powders with desirable morphologies. While this powder can be achieved at lower calcination temperatures, ceramics made from these techniques still require high sintering temperatures [55]-[57]. Moreover, this prior work did not rigorously verify the completeness of the reaction. Phase purity was only examined using XRD, which is not sufficient for determining the presence of inhomogeneity. Unfortunately these methods also often lack the simplicity inherent in solid state synthesis methods.

A synthesis method that incorporates BT (rather than BC) into the starting powder reactants would provide a more direct route to obtaining BXT. A BT based synthesis method would require a less intense calcination procedure, allowing for higher quality powders to be produced from solid state synthesis techniques. This will allow for reduced densification temperatures, leading to a finer control of the final ceramic microstructure. An expanded control of the microstructure will facilitate the development of transparent EO BXT.

In this chapter a BT based synthesis method is presented. This method involves using a mixture of $BaTiO_3$ (86.35 wt%), $CaCO_3$ (6.54 wt%), ZrO_2 (5.37 wt%), and TiO_2 (1.74 wt%) powders to synthesize BXT. Powders from this method were densified using CAPAD and compared to CAPAD densified samples made with BC based powders. The completeness of the BXT reaction was examined using a variety of techniques. From this, the qualitative level of inhomogeneity will be linked to sample properties. It will be shown that a BT based synthesis method allows for a substantial reduction in densification temperature over BC based methods, while still producing phase pure BXT ceramics.

4.1.1-Experimental Procedure

BXT powders were prepared using a solid state synthesis method. BC based BXT powder was prepared using $BaCO_3$ (99.9% MTI Corp., Richmond, CA, USA), $BaZrO_3$ (99% Alfa Aesar, Ward Hill, MA, USA), $CaCO_3$ (98% Reade Advanced Materials, Reno, NV, USA), and TiO_2 (99.9% Alfa Aesar). BC based BXT powder was prepared using $BaTiO_3$ (99.95% Inframat Advanced Materials, Manchester, CT, USA), ZrO_2 (ppm impurity, Tosoh Corporation, Tokyo, Japan), $CaCO_3$ (98% Reade Advanced Materials), and TiO_2 (99.99% MTI Corp). Both synthesis methods are mixed by first hand milling the components in a mortar and pestle and then tumble ball milling for 6 hours in ethanol. A summary of the powders used in this study can be seen in Table 4.1.

Table 4.1: Summary of individual chemicals used in both BC and BT based BXT synthesis techniques.

Powder	**Supplier**	**Size (nm)**	**Purity (%)**	**Weight %**
BC-Based Method				
BaZrO3	Alfa Aesar	1000	99	10.53
BaCO3	MTI	50	99.9	56.37
CaCO3	Reade	80	98	5.72
TiO2	Alfa Aesar	32	99.9	27.38
BT-Based Method				
ZrO2	Tosoh	25	ppm impurity	5.37
BaTiO3	Inframet	50	99.95	86.35
CaCO3	Reade	80	98	6.54
TiO2	MTI	30	99.99	1.74

Calcination conditions for the two synthesis methods should differ substantially due to the differences in carbonate content. Temperature dependent weight loss was measured using a TA Instruments Q600 Thermogravimetric Analysis (TGA) instrument (TA Instruments, Inc., New Castle, DE). For each measurement, 30 mg of powder was heated at 10 °C/min in dry air up to 1300 °C. From this analysis (presented below), along with some trial and error, a calcination temperature of 1000 °C for 18 hours was selected for the BC based powders while the BT based powders were calcined at 850 °C for 1 hour.

Powders made using both synthesis methods were densified using the CAPAD technique. BC based powders were densified at temperatures between 1200-1300 °C. For this set of samples, temperature was measured using an optical pyrometer aimed at the center of the die. BT based powders were densified between 1000-1200 °C. For this synthesis method, temperature was measured using an N-type thermocouple inserted in a hole drilled halfway through the die. All samples were processed at temperature for 5 minutes under 100 MPa of pressure. A heating rate of 200 °C/min and a cooling rate of 50 °C/min were used.

The as densified samples were annealed in air at 750 °C for 12 hours to eliminate oxygen vacancies created from the reducing atmosphere in the CAPAD. Samples are then polished metalographically using diamond to 1 μm. Density was determined using the Archimedes method. All microstructural analysis was performed using a XL-30 Scanning Electron Microscope (Philips, Eindhoven, The Netherlands). For BC based ceramics, grain size was determined from polished surfaces etched with HCL. Fracture surfaces were used to determine the grain size of BT based ceramics.

Phase homogeneity was examined on polished surfaces using the SEM in back-scatter electron (BSE) mode. A BT based sample processed at 1000 °C was further polished using Focused Ion Beam (FIB) milling from a FEI Quanta™ 3D 200i (FEI, Hillsboro, OR). XRD was also done on samples and powders using a PANalytical Empyrean (PANalytical, Almelo, The Netherlands). Permittivity was measured using an HP 4284A LCR meter (Keysight Technologies, Santa Rosa, CA). For this measurement, samples were measured in a parallel plate capacitor configuration with silver paste as the electrodes. All measurements were done at room temperature with a measurement frequency of 1 kHz.

4.2-Results

4.2.1-Microstructure and Electronic Properties

Temperature dependent weight loss data from the TGA can be seen in Figure 4.1. As expected, the BC based mixture loses significantly more weight overall than the BT based mixture due to the BC mixture containing more carbonate. While the BT based mixture completely finishes decomposing at <800 °C, this is not the case for the BC based powder. Although the decomposition slows down dramatically at 900 °C, the BC based mixture continues to gradually lose weight as the temperature is increased. It should be noted that the sample size used in the TGA is very small (30 mg). Producing powder on the scale necessary for efficient CAPAD densification requires powder batches on the order of 10 grams. The decomposition of such large quantities of powder will be slower than the small samples sizes used in the TGA. It was for this reason that the exaggerated calcination conditions used in this study were chosen.

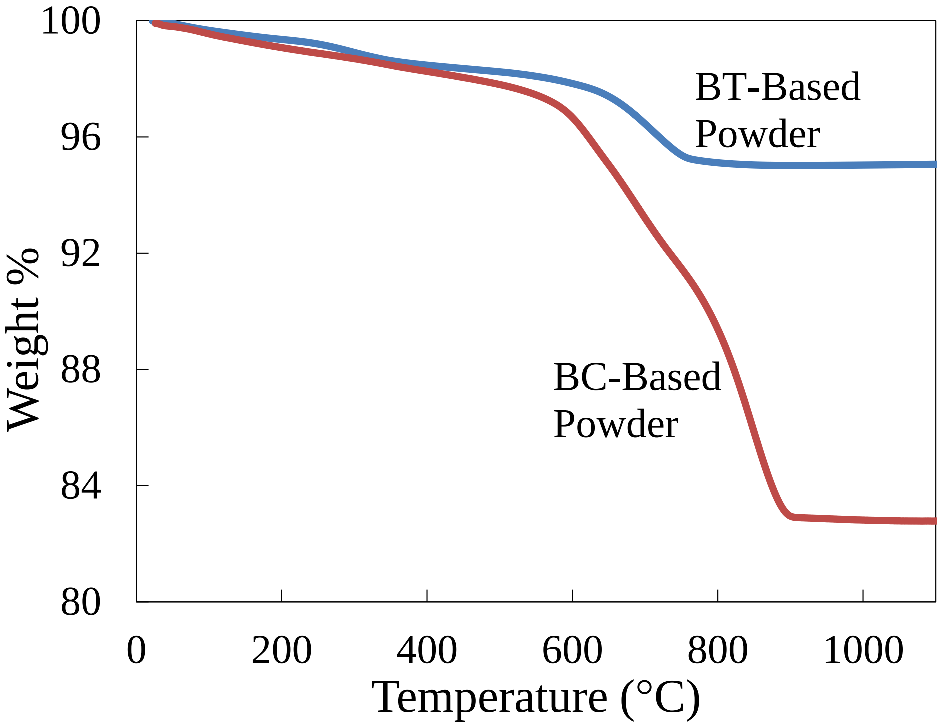

Figure 4.1: TGA data for both BC and BT based BXT powders.

All samples processed in this study possess a relative density of ≥99% based on Archimedes measurements. Permittivity versus CAPAD processing temperature for both BC and BT based samples can be seen in Figure 4.2. Permittivity increases with increasing processing temperature. This is expected, as permittivity is known to be very sensitive to processing conditions [58]. The largest permittivity achieved in this study is $\varepsilon = 3113$, from samples processed at 1300 °C. This is very similar to the permittivity achieved by Liu and Ren ($\varepsilon = 3060$) from free sintering BXT at 1500 °C [29].

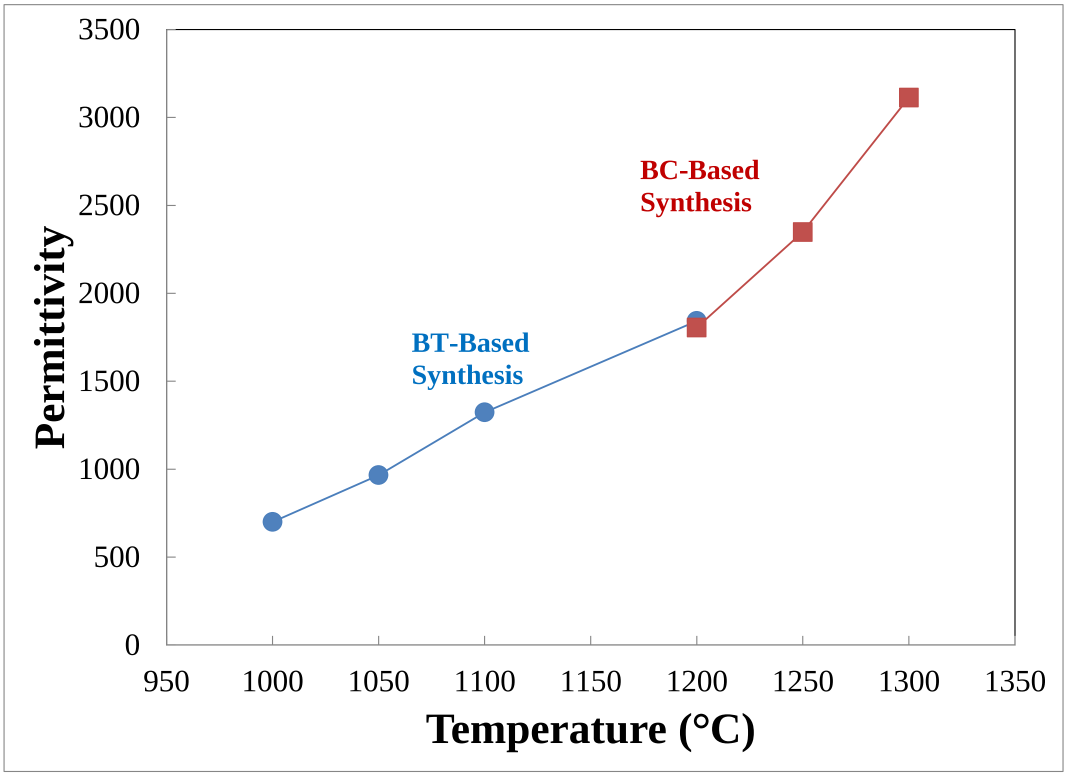

Figure 4.2: Permittivity vs. CAPAD processing temperature for both BC and BT based BXT ceramics.

A fracture surface micrograph of the 1000 °C BT based BXT sample can be seen in Figure 4.3. The grain size of this densified ceramic is in the range of ~100 nm. The reported grain size of the primary constituent of BXT, BT, is only 50 nm. This means that the grain size is effectively doubling during CAPAD processing. Such miniscule grain growth is not entirely unexpected. BT is known to be resistant to grain growth at similar temperatures [59].

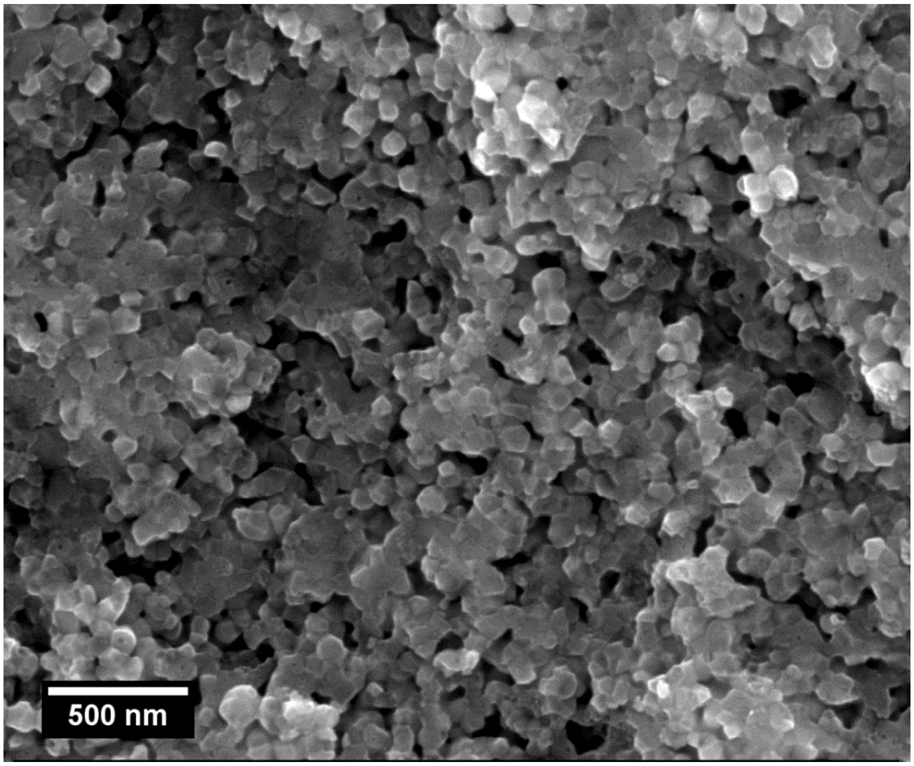

Figure 4.3: SEM micrograph showing a fractured surface of a BT based BXT ceramic densified at 1000 °C.

4.2.2-Phase Composition

XRD patterns for densified ceramics processed at different CAPAD temperatures and with different synthesis methods can be seen in Figure 4.4. All four patterns show the expected BXT perovskite phase. The BC based sample processed at 1200 °C shows extra peaks, corresponding to unreacted $BaZrO_3$ (BZO). The remaining three patterns show no extraneous peaks, implying phase purity.

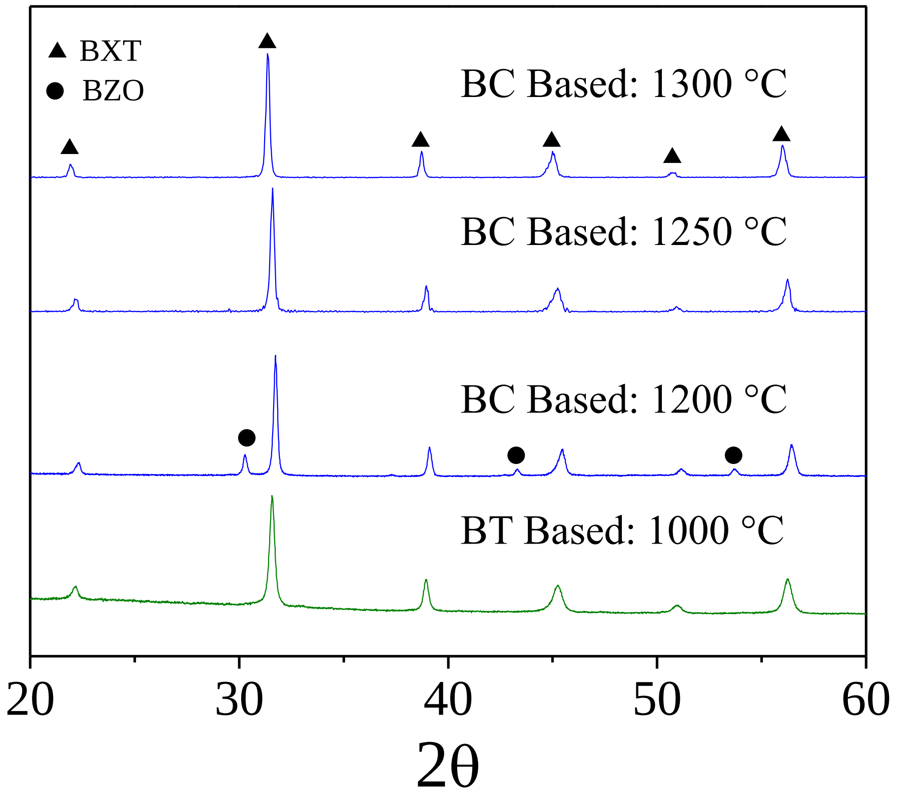

Figure 4.4: XRD patterns of densified ceramics processed at different CAPAD processing temperatures for BC and BT based BXT ceramics.

The SE and BSE micrographs for three samples densified at different temperatures using the BC based synthesis method can be found in Figure 4.5. As implied by the XRD data, samples densified at 1200 °C show visible inhomogeneity. Somewhat surprisingly, samples densified at 1250 °C also have a small amount of inhomogeneity. Samples densified at 1300 °C show no sign of inhomogeneity. The SE and BSE micrographs for a 1000 °C BT based sample can be seen in Figure 4.6. It can be seen that the BT based synthesis method produces fully reacted ceramics, even as low as 1000 °C. The color variation seen in the micrographs is due to topographical artifacts created during the FIB process.

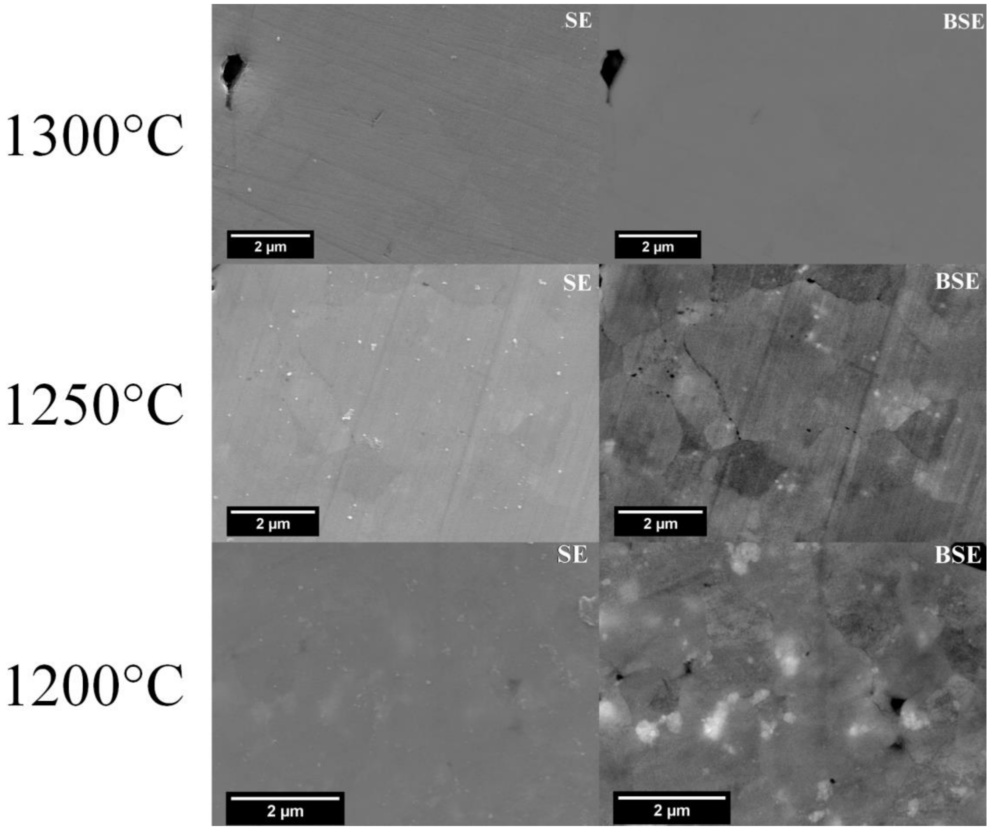

Figure 4.5: SE and BSE micrographs for BC based BXT ceramics processed at various temperatures.

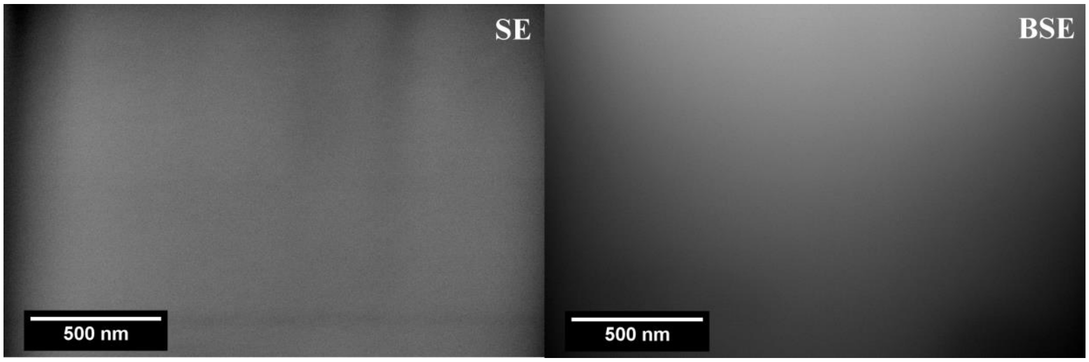

Figure 4.6: SE and BSE micrographs showing a FIB polished surface of a BT based BXT ceramic processed at 1000 °C.

4.3-Discussion

Due to the complex reaction path involved, BC based BXT requires a high processing temperature to produce a sample free of inhomogeneities. Based on the BSE micrographs in Figure 4.5, it can be seen that 1300 °C is required to form fully homogeneous BXT with this synthesis method. While XRD indicates phase purity at 1250 °C, BSE shows that inhomogeneities still exist in the densified ceramic. It is therefore apparent that XRD alone is not sufficient to determine microscopic phase purity. The presence of these inhomogeneities is sufficient to render BC based samples processed at 1250 °C or lower completely opaque. While some translucency is possible at 1300 °C, such temperatures are too high to retain the microstructural features necessary to make BXT transparent.

Conversely, ceramics densified using the BT based synthesis method demonstrate phase purity at temperatures as low as 1000 °C. This can be seen with both XRD and BSE microscopy (Figure 4.6). BT based samples are fully dense and completely homogeneous at temperatures 300 °C lower than what is required for BC based ceramics. Remarkably, this is also a full 500 °C lower than the commonly used free sintering temperatures (1500 °C). All of the BT samples produced in this study also demonstrate some optical translucency. This very low temperature provides a large degree of flexibility in processing conditions, which is necessary for controlling the microstructure of a polycrystalline ceramic.

It can be seen from Figure 4.2 that the permittivity of BXT depends heavily on processing temperature. This is not unexpected, and has been reported before in other studies on CAPAD processed BXT [60]. These studies attribute the decrease in permittivity to changes in grain size. It is believed that smaller grain sizes increase the prevalence of interference from the space charge layer [61]. Previous studies involving CAPAD densified BXT have produced samples with varying densities. Conversely, the densities of all the samples in this study are ≥99%, so the electrical property variations of the ceramics are not due to density (porosity). Instead other microstructural factors must be responsible. A summary of all of the samples produced in this study and their properties can be seen in Table 4.2.

Table 4.2: Summary of BC and BT based BXT samples produced in this study and their relevant properties.

Temperature (°C)	% Density	Reaction	Permittivity	Optical Quality
BC-Based Method				
1200	99	Incomplete	1805	Opaque
1250	99	Incomplete	2348	Opaque
1300	99	Complete	3113	Translucent
BT-Based Method				
1000	99	Complete	698	Translucent
1050	99	Complete	966	Translucent
1100	99	Complete	1323	Translucent
1200	99	Complete	1843	Translucent

BT based BXT shows a gradual increase in permittivity with increasing temperature. Since the BT based ceramics are all fully reacted, this change in permittivity can be attributed solely to the change in grain size. Conversely, BC based BXT shows a steep reduction in permittivity with decreasing temperature. This is likely due to the temperature influencing both the grain size and the level of homogeneity in the sample. It is apparent that the lack of phase purity adversely affects the permittivity of BXT, making the BC based synthesis method inadequate for low temperature processing. On the other hand, BT based synthesis allows for more flexibility when processing BXT. A large permittivity (ε = 698) can be achieved even at temperatures as low as 1000 °C using the BT based synthesis method. Moreover, BT based synthesis along with CAPAD densification at 1000 °C results in nanocrystalline (~100 nm), fully dense, and phase pure BXT ceramics.

4.4-Conclusions

The traditional BC based synthesis method has been shown to be adequate for producing high quality piezoelectric BXT [29]. Unfortunately, this synthesis method is insufficient for expanding BXT into additional functionalities (such as EO applications). This is due to the high processing temperatures required to complete the reaction to form BXT. The study presented here shows that using CAPAD processing, BC based BXT requires 1300 °C to fully react. Ensuring the completeness of reaction is critical for maximizing the properties of ferroelectric and optical materials. Both the transparency and permittivity are penalized heavily from the presence of inhomogeneities in the densified ceramics. Complete observation of the phase homogeneity can be difficult, as XRD is often insufficient at observing very small amounts of secondary phase.

A new synthesis method based on BT was developed to combat the challenges associated with BC based synthesis methods. This new synthesis method allows for the production of fully dense and fully reacted ceramics at temperatures as low as 1000 °C. These BT based polycrystalline ceramics possess no inhomogeneities and have a relatively high permittivity. The BT based synthesis method provides greater flexibility in processing parameters, allowing for greater control of the microstructure. This will be particularly important for achieving optically transparent BXT for EO applications (Chapter 5).

Chapter 5-EO Properties of BXT

5.1-Introduction

Although researchers have been successful in making BXT with excellent piezoelectric properties, so far the EO properties of BXT have not been explored. This is due to the difficulty associated with creating a microstructure that allows polycrystalline BXT to be transparent. The desirable piezoelectric properties of BXT strongly suggest that BXT will have a large EO response. Should transparency be achieved, BXT could prove to be a viable high performance lead free EO material.

Producing optically transparent polycrystalline materials requires very specific microstructural conditions. Said microstructures can only be produced with a combination of optimized powder synthesis and densification techniques. The previously outlined BT-based powder synthesis method produces powders that react and densify at temperatures substantially lower than what is required for the conventional BC based methods. Processing methods like CAPAD have the versatility necessary to maintain optimized microstructures.

In this chapter, a method for making transparent BXT ceramics will be presented. This method involves a combination of BT-based synthesis and CAPAD processing. The optical and EO properties of BXT will then be explored for the first time. It will be shown that BXT has extraordinary EO properties, far surpassing common state of the art materials. Through additional EO measurements, it will be shown that the EO properties of BXT are due to a complex field induced structural transition.

5.2-Experimental Procedure

Powders used in this method were mixed using the same procedure from the previous chapter. For this study, both BC and BT based powders were calcined at 1000 °C for 18 hours. Densified ceramics were produced using the CAPAD technique with a heating rate of 200 °C/min up to 1000 °C and then 25 °C/min up to 1200 °C. The samples were held at 1200 °C for 10 minutes under a pressure of 100 MPa. A cooling rate of 50 °C/min was used.

Densified samples were annealed in air at 750 °C for 12 hours and then polished with diamond slurry down to 1 μm. All microstructural analysis was performed using a XL-30 Scanning Electron Microscope (Philips, Eindhoven, The Netherlands). Grain size was determined from polished surfaces etched with HCL. Phase homogeneity was examined on polished surfaces using the SEM in back-scatter electron (BSE) mode. Samples and powders were analyzed with XRD using a PANalytical Empyrean (PANalytical, Almelo, The Netherlands). Crystal-structure analysis was performed on the measured XRD patterns using a full-pattern Rietveld refinement with MAUD [62].

An Uvisel M200 reflection ellipsometer (Horiba, Kyoto, Japan) was used to measure average refractive index, $\bar{n}$ and the extinction coefficient k in the wavelength range of 400–700 nm. With k, the optical band gap E_g could be found using the Tauc plot procedure [63]. The absorbance from this reflection based method, α_R can be found from the equation:

$$\alpha_R = \frac{4\pi k}{\lambda} \tag{5}$$

where λ is the wavelength of light. With this information, a Tauc plot can be constructed by plotting $(\alpha_R h\upsilon)^2$ versus $h\upsilon$ where h is the Planck constant and υ is the frequency of light. The value of *Eg* can be found by extrapolating the linear portion of this curve and finding the intercept.

The effective loss coefficient α_{eff} (a combination of scattering and absorption) was found using transmission data measured with a Cary 50 spectrophotometer (Agilent, Santa Clara, USA) in the range of 400–1000 nm. The value of α_{eff} was found using the equation

$$T = \left[1 - 2\left(\frac{\bar{n} - 1}{\bar{n} + 1}\right)^2\right] e^{-L\alpha_{eff}} \qquad 6$$

where *T* is the wavelength dependent in line transmission and *L* is the sample thickness. The value of $\bar{n}$ was extrapolated to 1000 nm using a single term sellmeier equation of the form [64]:

$$n^2 - 1 = \frac{S_0\lambda_0^2}{[1 - (\lambda_0/\lambda)^2]} \qquad 7$$

where S_0 and λ_0 are oscillator parameters.

BXT samples used for ferroelectric and electro optic measurements were electrically poled in oil at 2.37 MV/m for 1 hour. This poling condition was found by poling a sample under various conditions and measuring the EO coefficient. The conditions that produced the largest EO coefficient were used for the remainder of the study. Ferroelectric hysteresis data was acquired using the previously mentioned custom built Sawyer–Tower circuit. Samples were measured up to 2.6 MV/m in oil. The EO response of the samples was measured using the previously mentioned custom built senarmont compensator device. Bias field measurements were performed by increasing the applied field to 1.25 MV/m and back to zero. Each data point corresponds to the voltage difference between the local maxima and minima in light intensity. The data shown in this work was acquired after several continuous cycles.

5.3-Results

5.3.1-Microstructure and Phase analysis

A micrograph of the BT based powder after calcining and an additional tumble ball milling step can be found in Figure 5.1. It can be seen that minimal grain growth has occurred from the manufacturer reported starting grain sizes. There is noticeable agglomeration present throughout the powder. This is likely from the aggressive calcining conditions used in this study. The additional tumble ball milling step does not completely mitigate the agglomeration, indicating that more powder post processing is needed to optimize the powders.

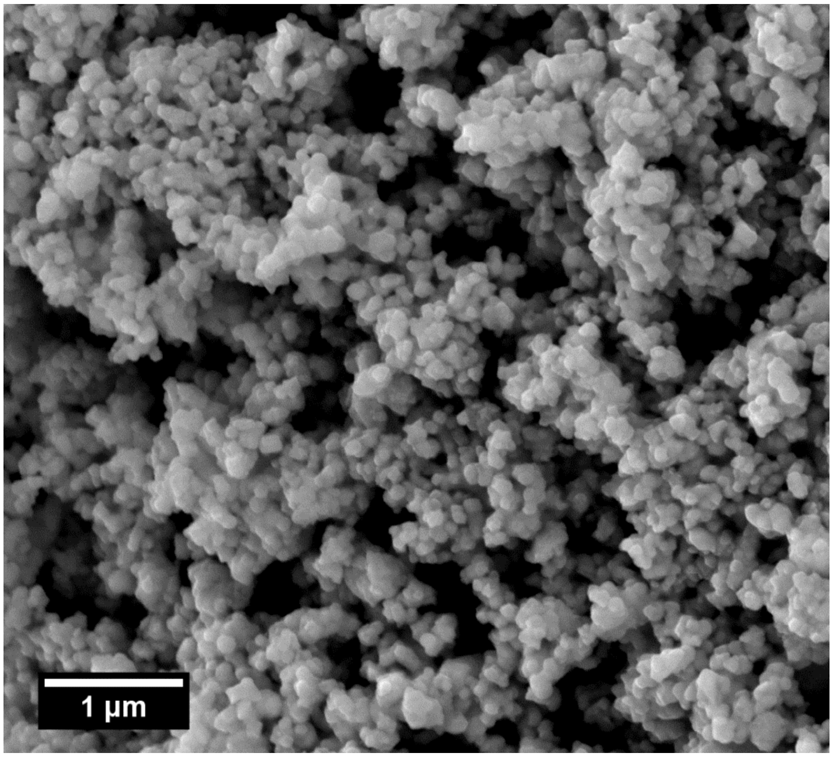

Figure 5.1: Micrograph of the BT based powder ready for CAPAD densification.

XRD patterns of powder and CAPAD-processed ceramics using the traditional (BC-based) and the new BT-based approaches can be seen in Figure 5.2. All patterns indicate a perovskite structure. The BC-based patterns, however, show additional peaks corresponding to unreacted $BaZrO_3$. In contrast, the BT-based patterns show only phase pure BXT.

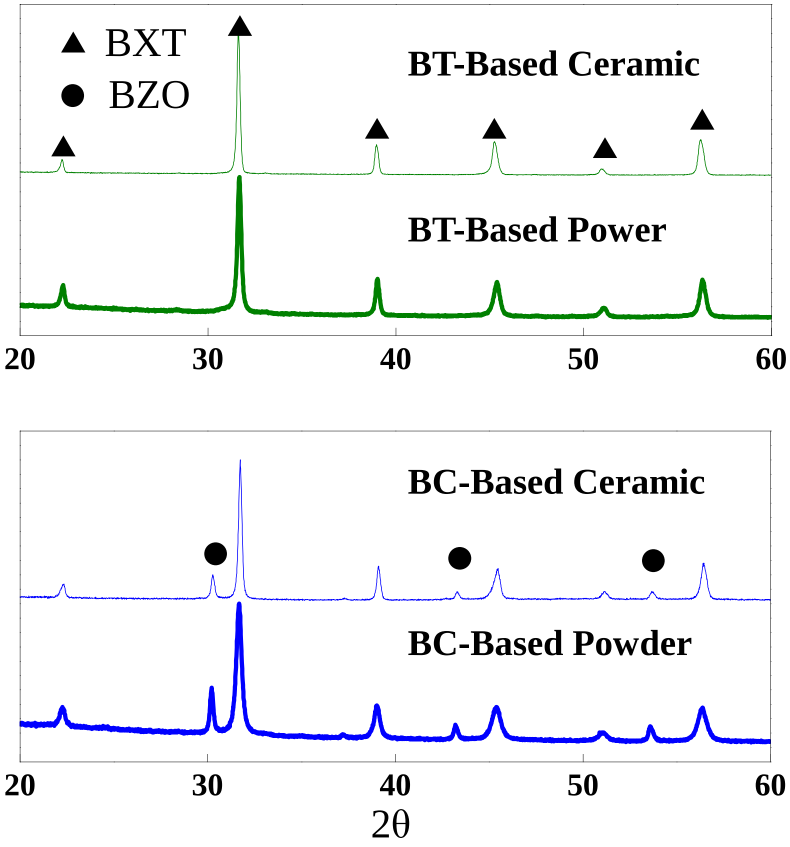

Figure 5.2: X-Ray diffraction patterns of powders and densified polycrystalline ceramics made using the BC and BT based methods.

SEM micrographs of the densified BC and BT based ceramics can be seen in Figure 5.3. BSE micrographs of the BC based densified ceramic confirm that it is not fully reacted. Conversely, the micrographs of the BT based sample shows a homogenous color, indicating a complete reaction down to the microstructural level. A SEM micrograph of an etched BT based ceramic can be seen in Figure 5.4. The average grain size for the densified BT based polycrystalline ceramic is 1.7 μm. This was calculated by averaging 600 grains.

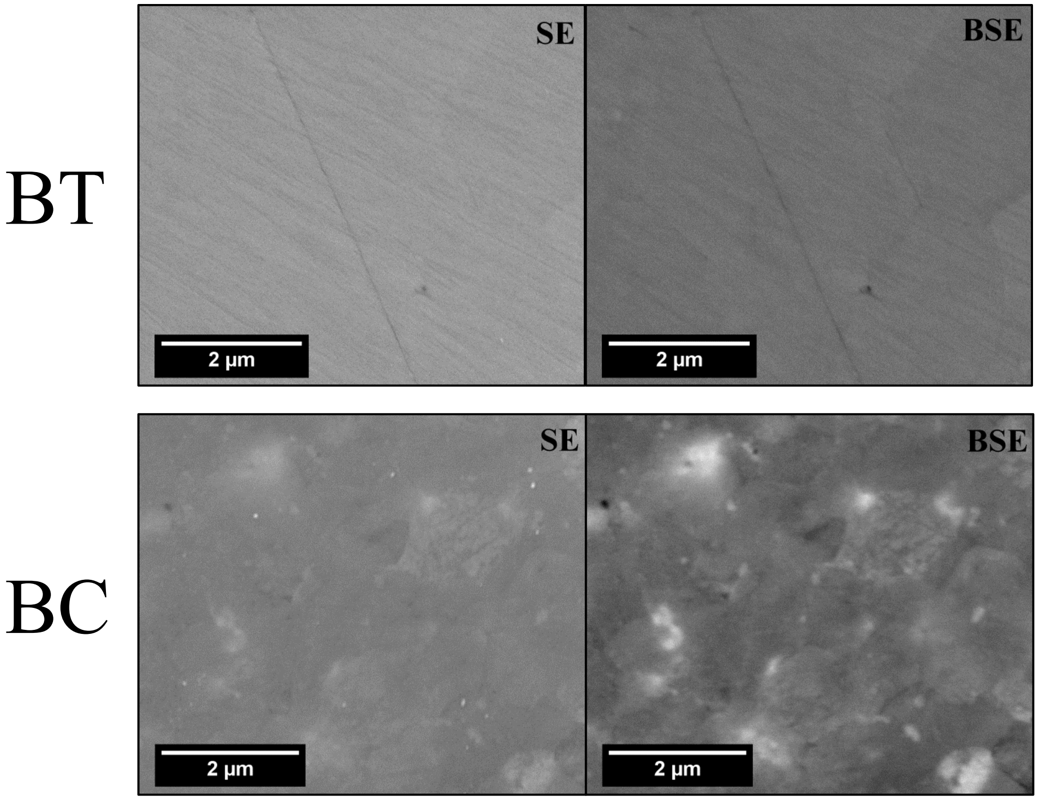

Figure 5.3: BSE and SE micrographs of the densified ceramics from both BT and BC based powder processes. Micrographs are of polished surfaces.

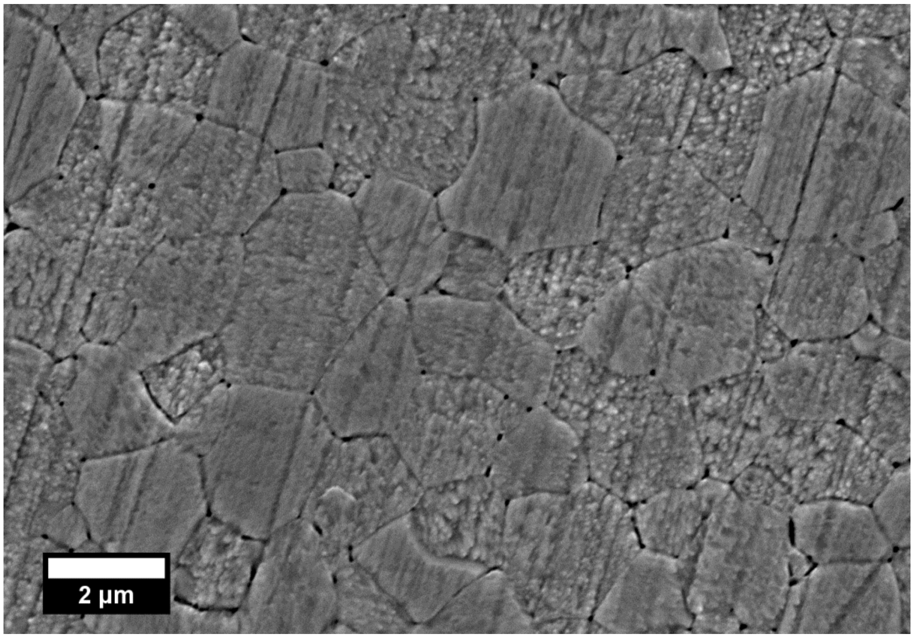

Figure 5.4: SEM micrograph of a densified BT based BXT polycrystalline ceramic. The surface was etched with HCL to facilitate grain size analysis.

5.3.2-Optical Properties

Percent transmission versus wavelength for a 0.55 mm thick densified BT based polycrystalline BXT can be seen in Figure 5.5. As expected, the transparency increases with increasing wavelength. Dispersion of the average refractive index of BT based BXT ceramics are presented in Figure 5.6. The refractive index also follows the common trend of decreasing with increasing wavelength. As implied by equation 3, the accurate measurement of the index of refraction is critical for determining EO properties due to its cubed relationship to r_c. For the wavelength used for the EO measurements (635 nm), BXT has a refractive index of $\bar{n} = 2.28$. This is comparable to the primary chemical constituent of BXT, $BaTiO_3$ ($n_1 = 2.36$, $n_2 = 2.4$) [65]. It is lower than PLZT ($\bar{n} = 2.5$)[66] and similar to LN ($n_1 = 2.2$, $n_2 = 2.28$) [67].

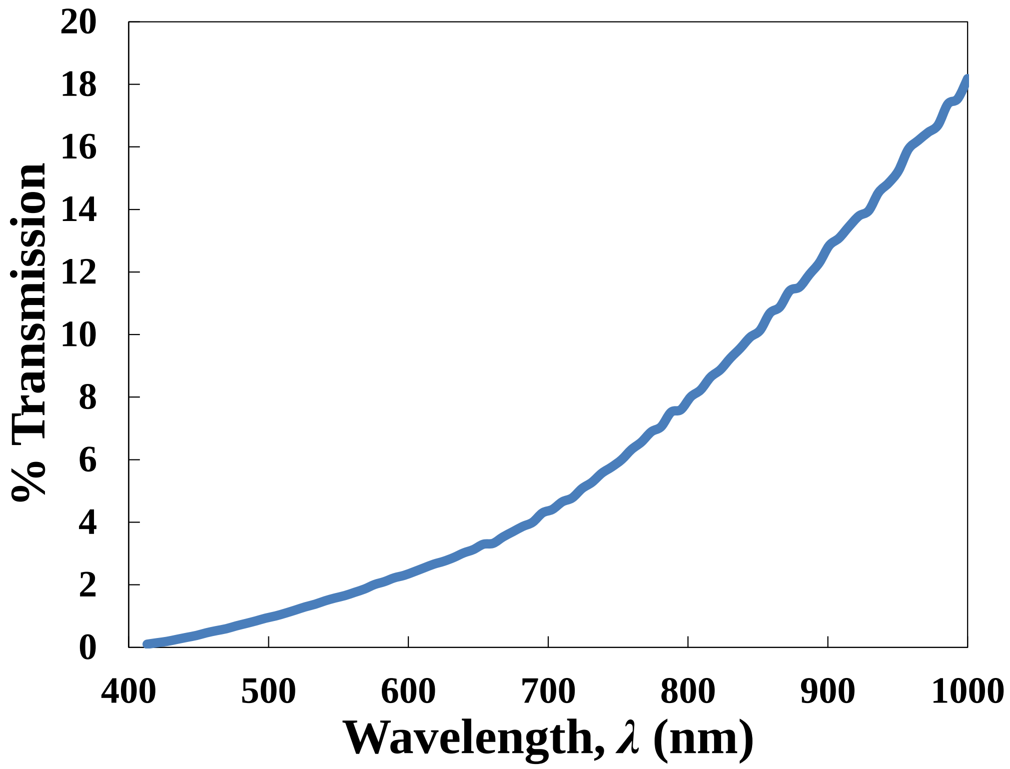

Figure 5.5: % Transmission versus Wavelength for a 0.55 mm thick densified BT based BXT ceramic.

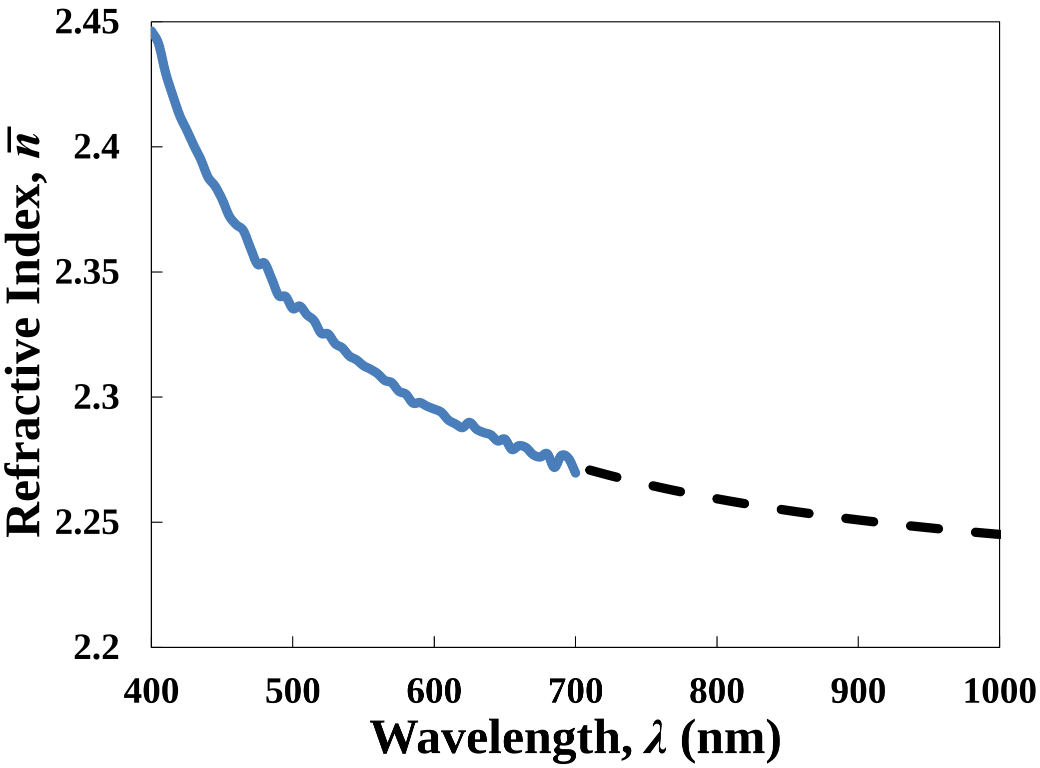

Figure 5.6: Dispersion of the average refractive index for BXT. The black dashed line shows where a Sellmeier fit was used to extrapolate the data.

5.3.3-Ferroelectric and EO properties

Ferroelectric polarization versus field measurements for a transparent BT-based ceramic can be seen in Figure 5.7. The coercive field for this sample is E_c = 0.34 MV/m while the remnant polarization is 0.05 C/m^2. These properties are in the range of values previously reported for BXT [29]. Observations in the literature show that coercivity and remanence can vary based on microstructural condition (i.e. grain size) and processing procedures [60].

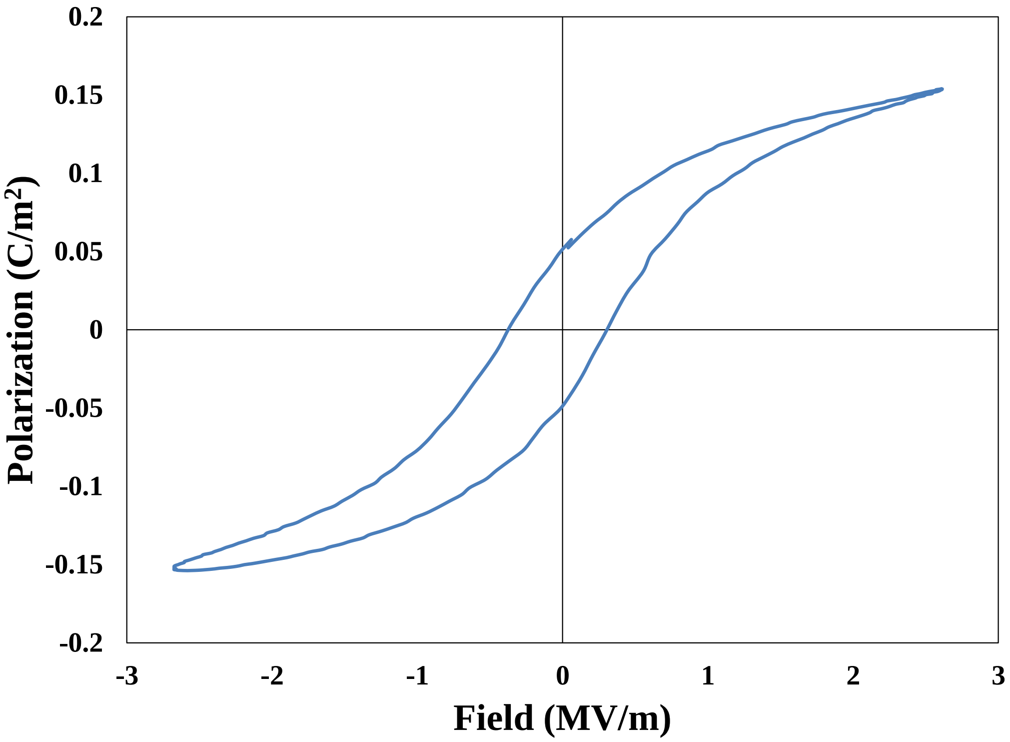

Figure 5.7: Ferroelectric hysteresis curve of polarization versus electric field for the BT-based BXT ceramic.

The raw data from the EO measurements are shown in Figure 5.8. This data demonstrates the custom built senarmont compensator being cycled with a 100 mHz (essentially DC) driving voltage between “off (zero)” to “on (one)” amplitude using a transparent BXT ceramic. A very low voltage ($V\pi$ = 370 V at a thickness of 0.55 mm) is required for modulation because of the remarkably high direct current (DC) r_c = 530 pm/V of the BXT ceramic. Even after repeated cycling, the EO effect in BXT is shown to be consistently high and repeatable. The effect of higher driving frequencies on the EO coefficient of BXT can be seen in Figure 5.9. At 10 kHz, BXT has an r_c = 425 pm/V, demonstrating that BXT maintains >80% of its DC r_c, even at frequencies as high as 10 kHz. A large high frequency EO coefficient is particularly important as most EO modulators are operated at relatively high driving frequencies.

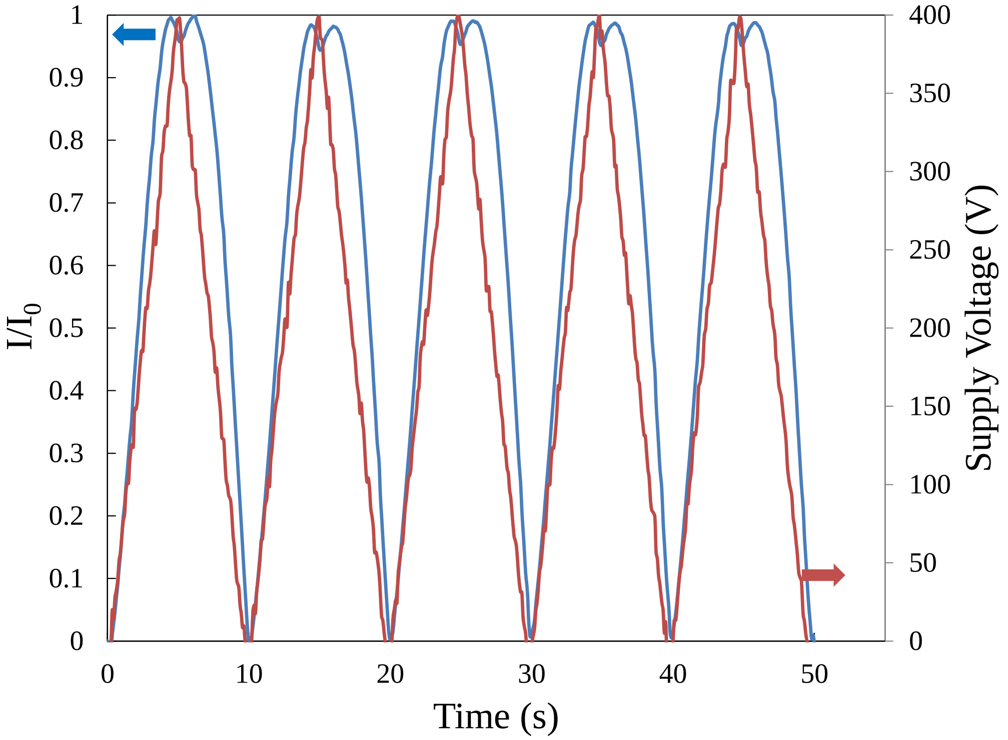

Figure 5.8: Raw data for multiple EO measurement cycles displaying intensity ratio and voltage versus time.

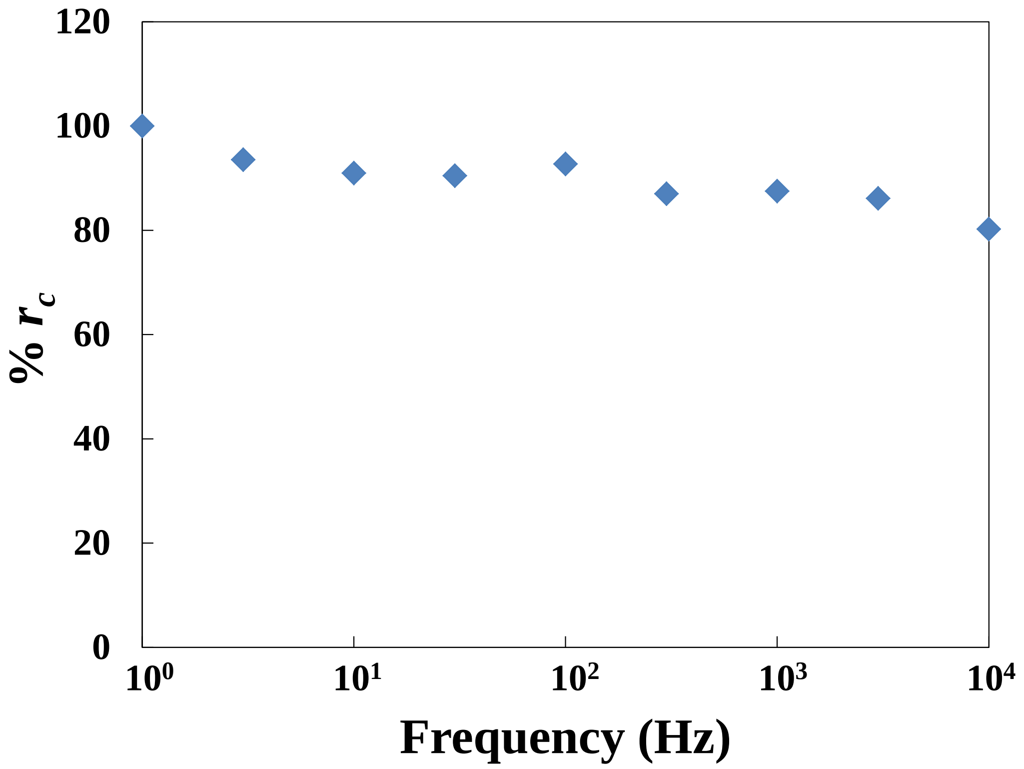

Figure 5.9: Relative EO coefficient versus driving frequency measured up to 10 kHz.

Poling conditions can have a major impact on ferroelectric properties, as has been previously seen in BXT [68][69]. Poling dependent EO data can be seen in Figure 5.10. A maximum in r_c occurs when BXT is poled at 2.37 MV/m for 1 hour. As expected lower poling times reduces the EO coefficient. Higher poling fields also do not guarantee an increased EO response. A similar “overpoling” response has been observed in the piezoelectric properties of BXT [70].

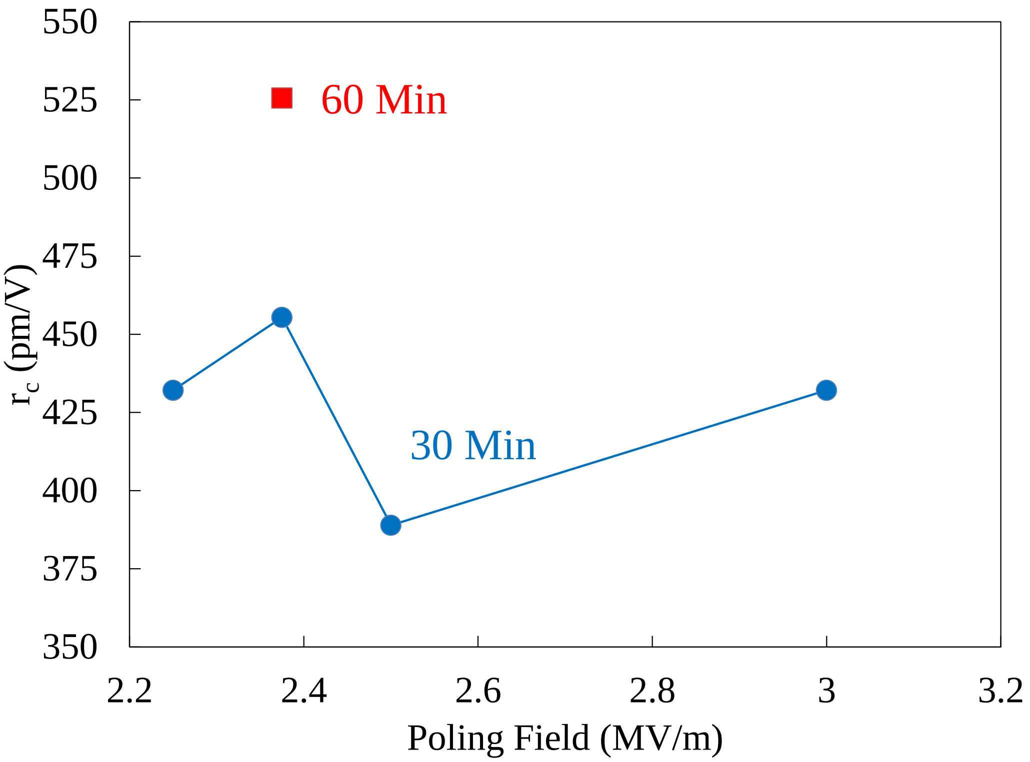

Figure 5.10: Poling dependent EO response for BT based BXT.

Bias-field results for BXT can be seen in Figure 5.11. Regions of interest, corresponding to changes in the active mechanism, are denoted with roman numerals. In the increasing direction, r_c increases with increasing bias field (region I and II) until a bias field of ~1 MV/m, at which point the EO coefficient starts to decrease (region III). In the decreasing direction, the results show that r_c increases from its initial value until ~0.8 MV/m (region III). The EO coefficient remains relatively unchanged until ~0.4 MV/m (region II), where a further decrease in bias field reduces r_c (region I).

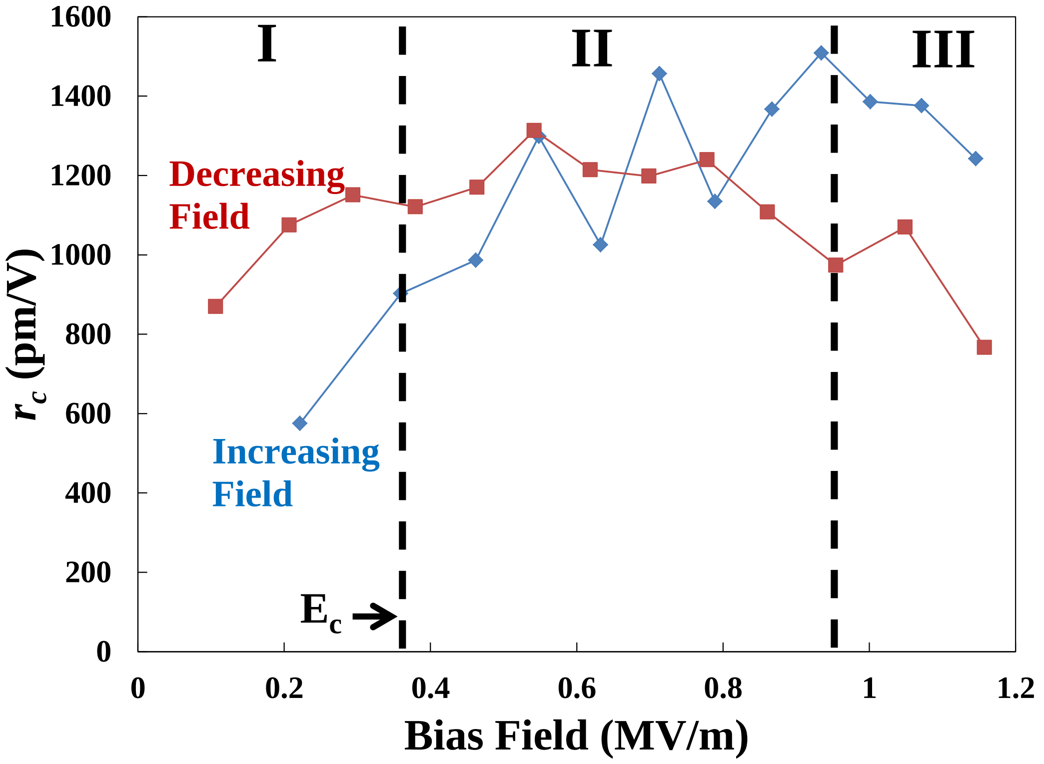

Figure 5.11: Bias field dependence of EO coefficient for both increasing and decreasing bias field.

5.4-Discussion

5.4.1-Microstructure and Phase Analysis

Both SEM and XRD data confirm that BC based BXT is inhomogeneous, while BT based BXT is completely reacted. As seen in Figure 5.12, CAPAD processed ceramics from the BT based synthesis route are transparent while samples made from the BC route are opaque. The transparency in the BT based sample is a result of a very high density (99+% determined from Archimedes method), full reaction and relatively fine grain size (average = 1.7 μm). From a synthesis point of view, one can see that BXT is ~86 wt% BaTiO3. BT-based powders require less overall reaction to form BXT since they do not need to form BT first. Furthermore, reducing the BC content will help the densification process by reducing gas evolution. The decomposition of a carbonate results in the release of CO and/or CO_2. An incomplete decomposition during calcination can cause these byproducts to be released during CAPAD processing, impeding densification. This is particularly important since full densification is needed to achieve transparency.

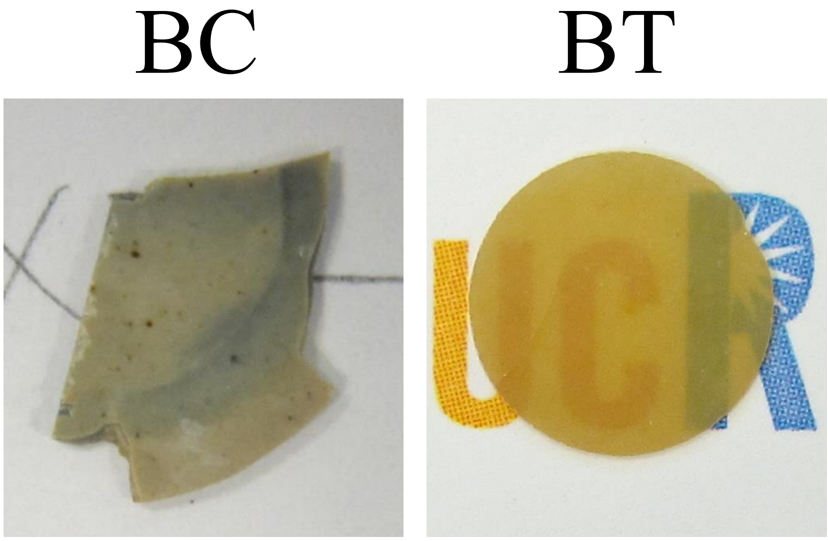

Figure 5.12: Photographs of BXT polycrystalline ceramics from BC and BT synthesis and densified using CAPAD.

BXT is known to have a mixture of tetragonal and orthorhombic phases. The amount of each phase present should have a profound impact on the properties of BXT. Rietveld refinement of the XRD patterns for the BT based densified ceramics indicates the presence of a mixed phase structure. A satisfactory fit occurred with a structure composition consisting of 38% tetragonal phase and 62% orthorhombic phase ($\chi^2 = 1.35$ and $R_{wp} = 6.03\%$). This result is in good agreement with the recent synchrotron measurements of BXT [33].

A histogram of the distribution of grain sizes in the BT based densified BXT can be seen in Figure 5.13. Grains as small as 0.3 μm in diameter and as large as 5 μm in diameter can be seen in the densified ceramic. While the distribution of grains in BXT does not appear to be bimodal, there is a wide distribution of grain sizes. The unimodal behavior of the distribution can be verified by seeing that the median (1.6 μm) lies between the mean (1.71 μm) and the mode (1.25 μm). The distribution is also skewed to larger grain sizes. Although obvious from the figure, this can be verified by seeing that the mean is larger than the median. Both values are also significantly larger than the mode.

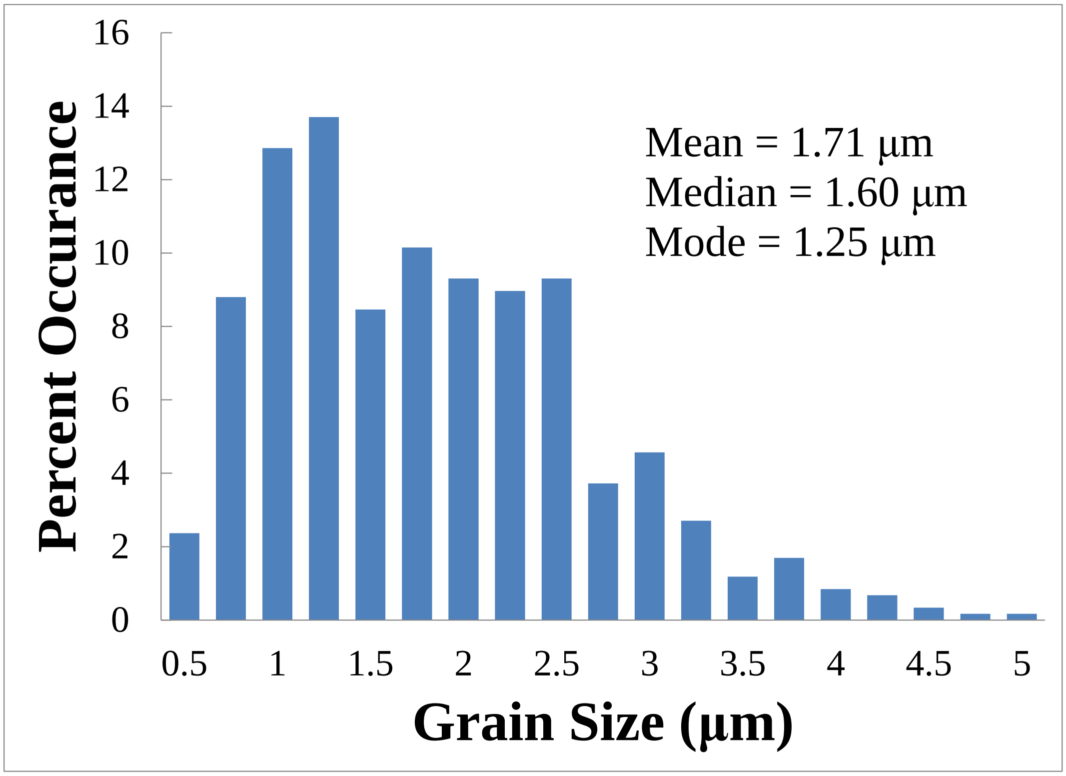

Figure 5.13: Histogram of grain size distribution in the BT based BXT ceramic densified at 1200 °C. Data is based on grain size measurements of etched polished surfaces

While large grains are not desirable for optical properties, the distribution of the grain sizes can provide valuable information about the ceramic and how to improve it. The wide distribution of grain sizes indicates the presence of some abnormal grain growth. The abnormal grain growth is likely from agglomeration in the powder. Figure 5.1 shows that the powder still has obvious agglomeration. Such agglomeration will produce abnormal grain growth and inhibit densification. Additional measures will need to be taken to deagglomerate the powder or to reduce the required calcining temperature.

5.4.2-Optical Properties

Using the extinction coefficient data from the ellipsometer, a Tauc plot can be constructed to determine the E_g for BXT. The Tauc plot can be seen in Figure 5.14. Based on the linear extrapolation (the solid black line), the measured bandgap for BXT is E_g = 3.6 eV. This is similar to the values for PLZT, which can have a bandgap of 3.35–3.67 eV (depending on composition and processing) [28][71]. BXT also has a comparable bandgap to $LiNbO_3$ (~4 eV) [72]. BXT has a larger band gap than its primary constituent, BT (E_g = 3.27-3.38 eV) [73]. Since the optical bandgap is larger than 3.1 eV, BXT is expected to transmit all visible wavelengths.

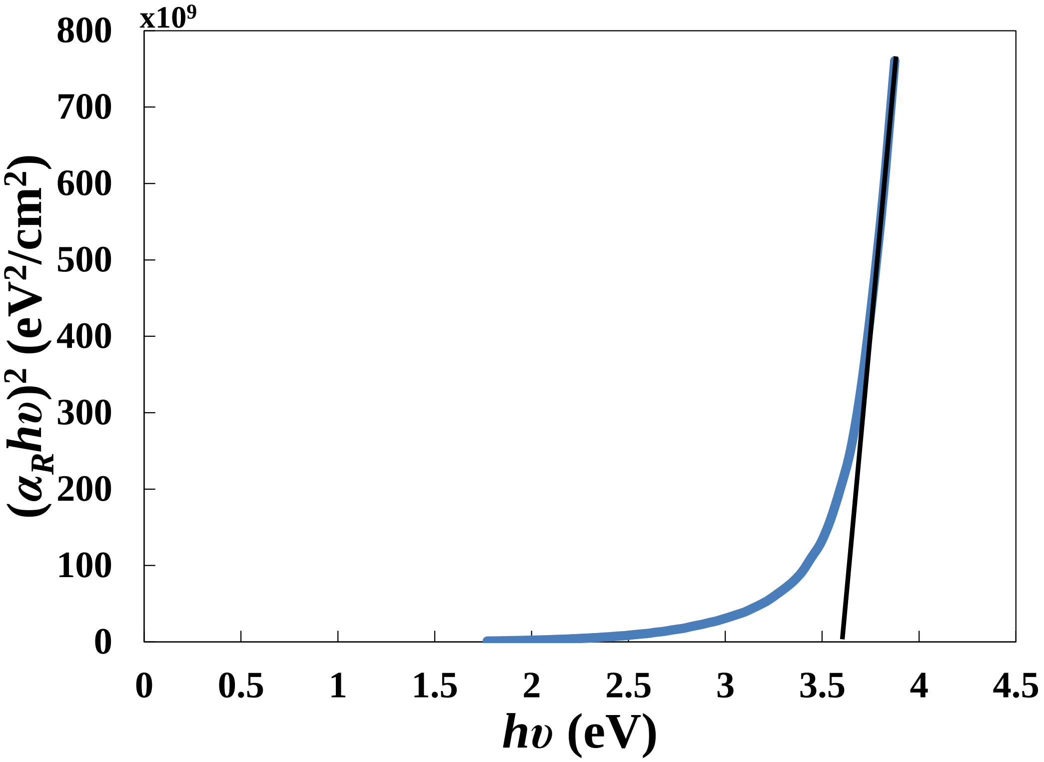

Figure 5.14: A Tauc plot for BXT calculated from the measured extinction coefficient (not shown). The solid black line indicates the extrapolation of the linear part of the curve, which is used to find the band gap.

The yellow color of the transparent BT based ceramic suggests that there are absorption centers (color centers) present in the lattice of the samples. BXT samples free sintered in air (not shown here) are also yellow in color (although not transparent). This suggests that the color is from impurities in the powder. Since the powders are mixed by low-energy ball milling, which should not cause meaningful contamination, it is likely that the impurities are from the original powders. The most likely source is the calcium carbonate ($CaCO_3$), as it has the lowest purity out of the starting powders (98% purity). The acquisition of higher quality $CaCO_3$ could eliminate the yellow color and potentially enhance the optical quality of transparent BXT.

In addition to absorption, scattering is also seen in the transparent BXT samples. This is likely due to the presence of small amounts of residual porosity, as well as the anisotropic structure. Using the refractive index and transmission data, the loss coefficient α_{eff} can be calculated from equation 6. The loss coefficient versus wavelength can be seen in Figure 5.15. As anticipated, α_{eff} decreases with increasing wavelength. At 635 nm, the densified BXT has an optical loss of 49 cm^{-1}. This is approximately one order of magnitude larger than nanocrystalline 8YSZ [74] and nanocrystalline Al_2O_3 [75] densified using the CAPAD method. Although the value of α_{eff} for BXT is relatively large, further optimization of the synthesis and processing methods should be able to reduce this value.

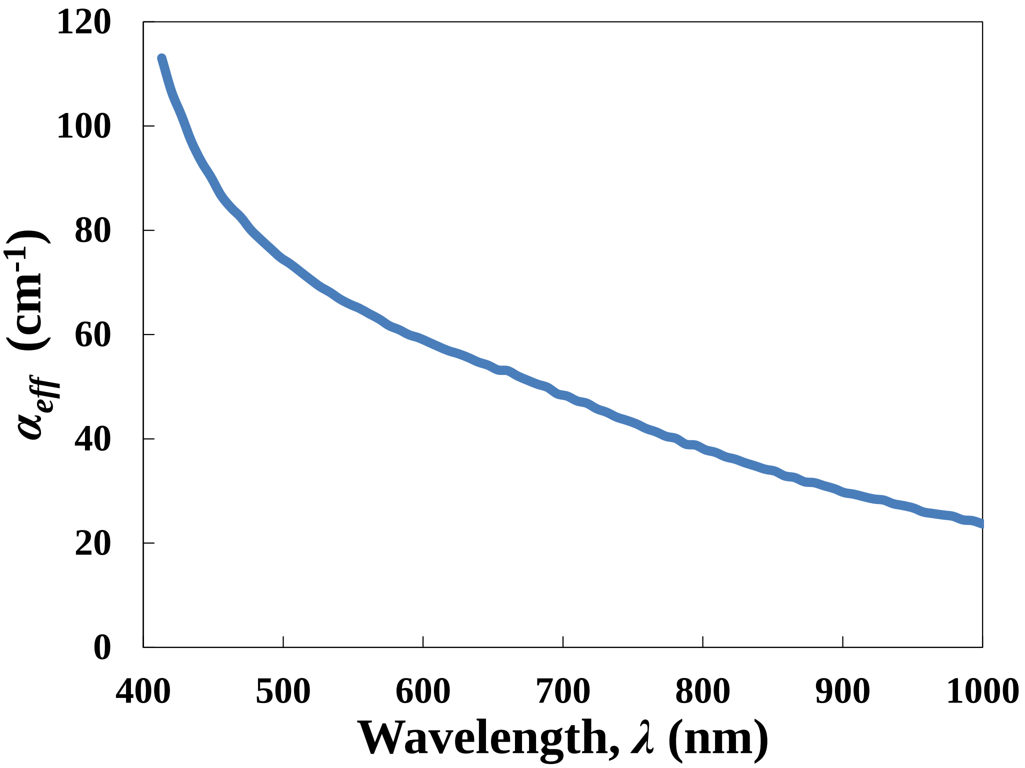

Figure 5.15: Effective optical loss coefficient versus wavelength calculated from the transmission and refractive index data.

As previously mentioned, α_{eff} contains both scattering and absorption contributions. Unfortunately, at this time it is not possible to de-couple the loss coefficient data into absorption and scattering. However for the purposes of discussion the loss coefficient data was further analyzed to glean possible scattering mechanisms. By assuming that the absorption contributions do not vary significantly with wavelength, further insight into the scattering mechanisms can be determined by analyzing the wavelength dependence of α_{eff}. Effective optical loss versus $1/\lambda^2$ (fitting to an RGD model) can be seen in Figure 5.16. The value of α_{eff} varies linearly with $1/\lambda^2$, especially at higher wavelengths. This indicates that the scattering is controlled by the anisotropic crystal structures in BXT. There is some deviation at lower wavelengths, indicating that porosity may play a role as well. This can be seen more clearly by examining optical loss versus $1/\lambda^4$ (fitting to a Rayleigh model) as shown in Figure 5.17. While there is deviation at the higher wavelengths, there is some linearity at the lower wavelengths. This indicates that porosity still plays some role in the optical properties of these BXT ceramics. Further optimization of the microstructure will be necessary to reduce the influence of porosity and reduce the grain size.

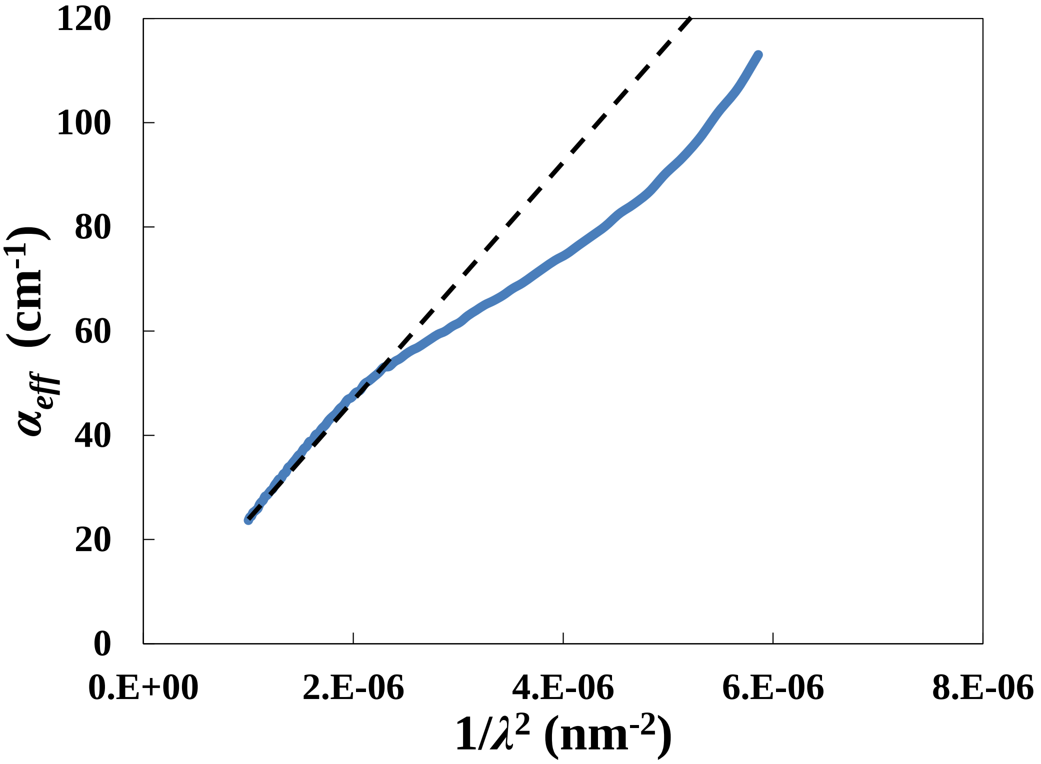

Figure 5.16: Effective optical loss coefficient, α_{eff} vs $1/\lambda^2$ showing the applicability of the RGD approximation. Dashed lines are to demonstrate linear fitting.

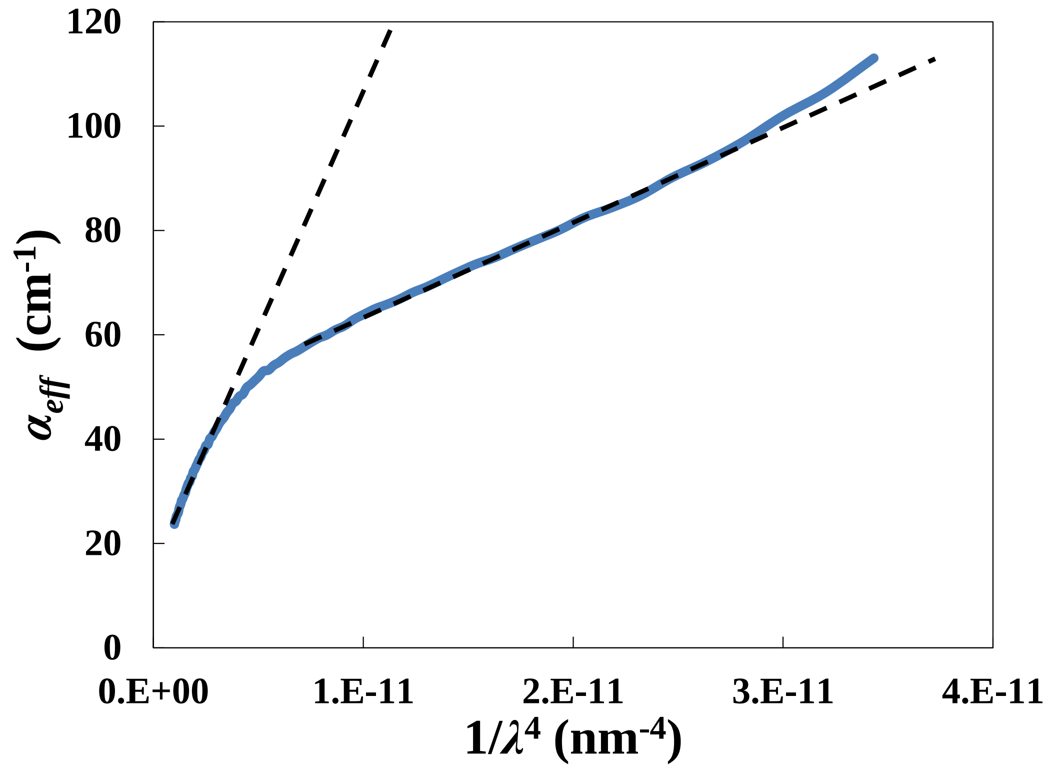

Figure 5.17: Effective optical loss coefficient, α_{eff} vs $1/\lambda^4$ demonstrating the applicability of the Rayleigh approximation. Dashed lines are to demonstrate linear fitting.

5.4.3-EO properties

Many high-performance EO materials, such as PMN-PT and certain kinds of PLZT, are relaxor ferroelectrics (not displacive) [76]. Such materials possess a quadratic response to electric field and a highly reduced EO coefficient at high driving frequencies [77]. Figure 5.8 demonstrates that the EO effect in BXT is repeatable, consistent, and linear with applied voltage. Figure 5.9 demonstrates that the large EO effect in BXT is maintained at high driving frequencies. Together these two figures indicate that the EO effect in BXT is not relaxor in nature. This result is consistent with the displacive ferroelectric nature of BXT found in the literature, except what relaxor behavior is expected from microstructural influences [60].

The reduction of r_c with increasing driving frequency seen in BXT is likely due to the relatively slow response of some domain phenomena. This kind of reduction is seen in other EO materials that rely on domain related phenomena, such as thin-film $BaTiO_3$ [78]. Single-crystal $BaTiO_3$ loses ~3/4 of its DC r_c value under high-frequency clamping conditions [79] and thin-film $BaTiO_3$ measurements show that the r_c at 10 kHz is about 1/2 of the DC r_c [78]. Common forms of PLZT also show a dramatic decrease in EO response with frequency; the r_c at 10 kHz is less than half of the DC value [77].

Since the EO effect in LN is not dominated by domain switching effects, it is stable even at very high frequencies up to the GHz range [80]. Even though LN has a relatively low EO coefficient, it is still the material of choice for very high frequency applications. Additional EO experiments will be necessary to determine the viability of BXT for higher frequency applications. In the frequency range reported in this work (up to 10 kHz), the r_c of BXT is higher than LN, BT, and PLZT.

A comparison of the r_c of BXT with other EO materials can be seen in Figure 5.18. The EO coefficient for BXT (r_c = 530 pm/V) is 26.5 times higher than the state-of-the-art material LN (r_c = 20 pm/V) [25]. This value is significantly larger than the standard high-performance EO materials $BaTiO_3$ (r_c = 96 pm/V [79]) and PLZT ($Pb_{0.88}La_{0.12}(Zr_{0.4}Ti_{0.6})_{0.97}O_3$, r_c = 136 pm/V [81]). These previously referenced EO coefficients were chosen because they were measured using low-frequency Senarmont compensator techniques at a similar wavelength to this study (~635 nm). To the authors' knowledge, the value measured in this work is the highest linear EO coefficient of any ceramic displacive ferroelectric material in the frequency range investigated. A summary of the refractive index, band gap, and EO coefficient for these materials can be found in Table 5.1 for reference.

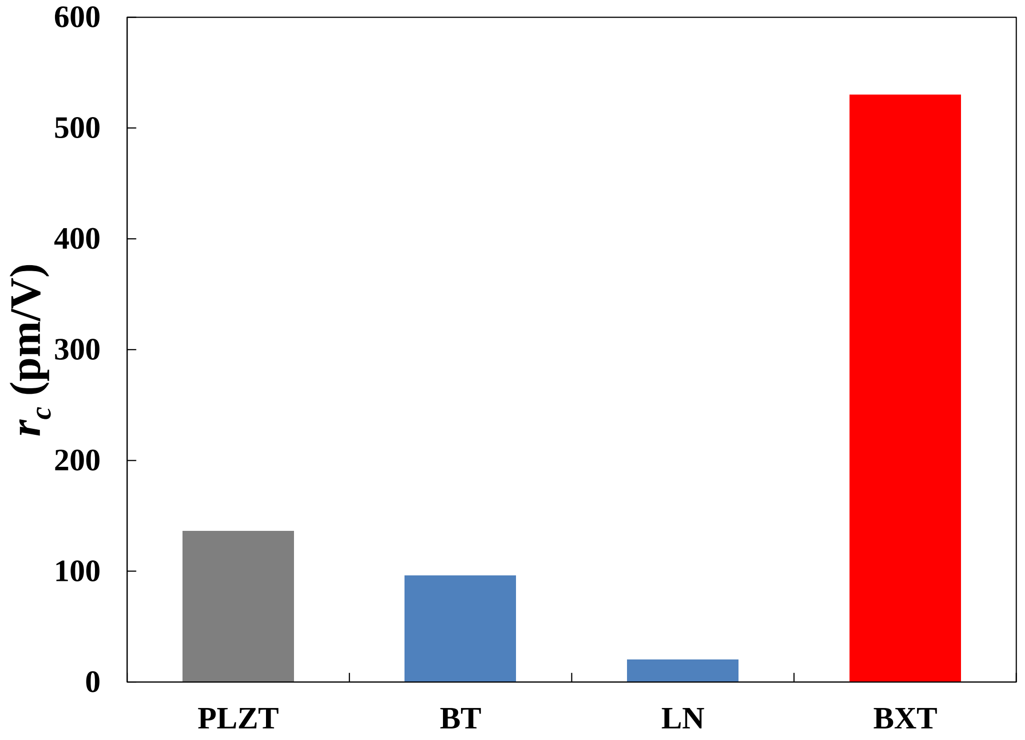

Figure 5.18: Bar chart comparing the EO coefficient of BXT to other common lead based and lead free EO materials.

Table 5.1: A summary of all the relevant properties for the previously discussed EO materials. References are given in the text above.

Material	$\bar{n}$	E_g **(eV)**	r_c **(pm/V)**
BXT	2.28	3.6	530
$LiNbO_3$	2.2, 2.28	4	20
$BaTiO_3$	2.36, 2.4	3.27-3.38	96
PLZT	2.5	3.35-3.67	136

A large EO coefficient offers significant flexibility in the design of EO devices. Transparent BXT will allow for miniaturized EO devices that require reduced operating voltages. Figure 5.19 shows a to scale comparison of the thickness of the materials needed to cause the same EO rotation given the same applied field. If one desires an EO modulator that operates at the same V_π as the one based on a LN crystal, the length of the BXT ceramic required is 26.5 times smaller than the required LN crystal. Similarly, when the dimensions of BXT and $LiNbO_3$ are the same, BXT offers an incredible 26.5 times reduction in V_π. This can be seen in Figure 5.20, where the calculated EO response (based on Equation 3) is shown assuming identical sample dimensions (L = 0.55mm and d = 2mm). The response of $LiNbO_3$ cannot be properly displayed due to the very high voltages required. The use of BXT allows for a 26.5 times reduction in V_π when compared to a $LiNbO_3$ crystal of the same dimensions.

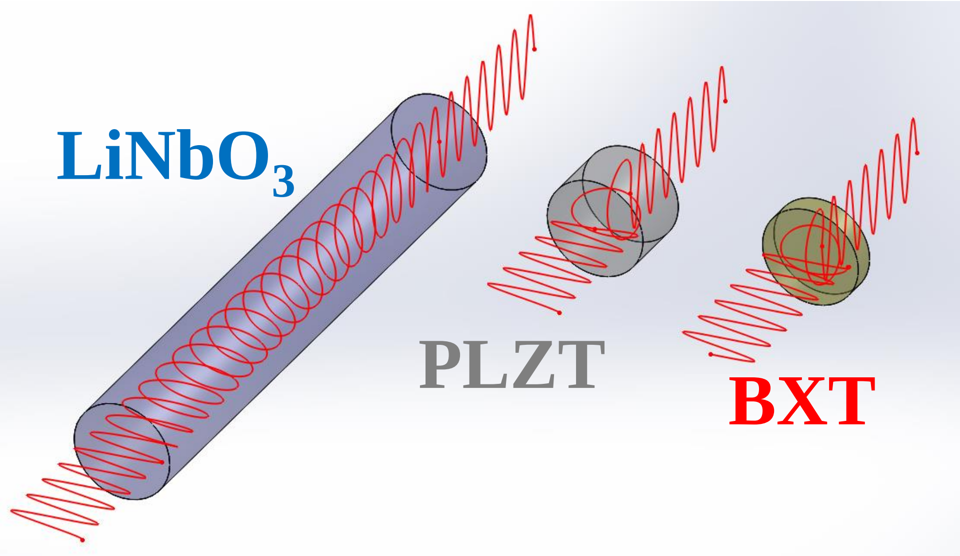

Figure 5.19: A schematic comparison of material thickness required to achieve the same EO rotation. Thicknesses are drawn to scale assuming the same value of V_π is desired.

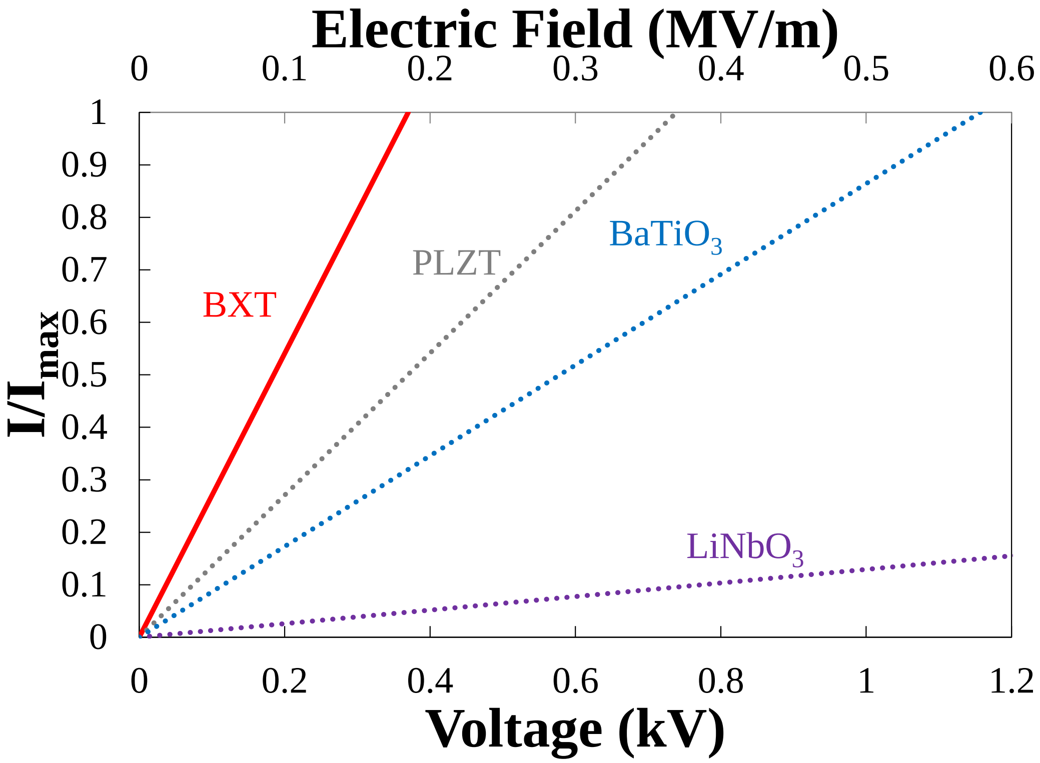

Figure 5.20: Calculated EO response of various EO materials assuming identical sample geometries. Data for LiNbO$_3$ is truncated for clarity.

5.4.4-Field Induced Structural Evolution

As mentioned previously, the EO response can be affected by ferroelectric and ferroelastic domain conditions [18]. The ferroelectric results in Figure 5.7 show that the transparent BXT in this study has a coercive field of E_c = 0.34 MV/m. Based on the geometry of the sample used in the EO measurements, the measured V_π = 370 V corresponds to an operating field of E_π = 0.185 MV/m. Since fields near E_c are where domain activity is at its highest, the proximity of E_π to E_c would indicate that the EO properties of BXT are controlled by domain motion. It is important to note, however, that while BT commonly possesses coercivities on the order of $\mathrm{E_c}$ = 0.3-0.5 MV/m [82], the EO properties of BT are only r_c = 96 pm/V. Were the EO properties of BXT completely controlled by domain activity, BXT would likely have an EO coefficient very similar to BT. This indicates that the EO properties in BXT are not entirely determined by domain motion. Other mechanisms must be contributing.

The XRD results discussed previously confirm the presence of orthorhombic (O) and tetragonal (T) phases. These two phases have very different optical symmetries (the tetragonal phase is uniaxial while the orthorhombic phase is biaxial). The interplay between orthorhombic and tetragonal domains and their field evolution should be critical to the EO response in BXT. A proper interpretation of the bias field results found in Figure 5.11 will shed light on the influence that the domain and phase activity has on the EO properties.

Even at low electric fields, region I displays a considerable change in the EO coefficient. Perhaps most importantly, region I encompasses the coercive field (E_c = 0.34

MV/m in this study). This represents the field where domain switching becomes most active. This low-field EO response result aligns well with the findings of the Xiaoli Tan group [83] . Through careful in situ TEM analysis, it was shown that BXT can form a unique single domain state during poling, indicating that BXT is capable of considerable domain switching even under low applied field. Although common for single crystals, a single domain state was unheard of in polycrystalline ceramics until its discovery in BXT. This single domain state occurs at electric field strengths near the coercive field. Further insight was provided by Acosta et al, who deconstructed the piezoelectric effect in BXT into intrinsic (lattice) and extrinsic (domain switching) contributions [84]. This was done with bias field piezoelectric measurements. It was found that most of the piezoelectric effect in BXT comes from domain-switching phenomena. The dramatic change in the EO effect in region I can therefore be attributed to the increasingly efficient domain switching as the electric field approaches and exceeds the coercivity.

Increasing the electric field into region II results in a continued increase in the EO coefficient. This increase in r_c is sustained over a large electric-field range. From in situ TEM work, it was shown by Guo et al. that the single domain state disappears at higher electric fields, forming a multidomain state [85]. This allows for domain activity to continue contributing to the EO effect in BXT. While efficient domain switching will account for some increase in EO response, the aggressive increase in r_c in BXT cannot be solely explained by this. Were the domain motion the only mechanism active in BXT, the EO coefficient would be expected to plateau in region II. An additional mechanism must be contributing to the increasing EO activity.

It is likely that an electric field-induced phase transition is occurring in concert with the domain activity. In situ X-ray diffraction experiments by Guo et al. show that the orthorhombic content in BXT increases under applied fields [85]. Such a result is not unprecedented, as similar work shows that multiphase ferroelectric materials have a tendency to transform to lower symmetry phases under applied field. For example PZT [86] and KNN [87] transforming to a monoclinic phase under applied field.

Optically speaking, a transformation from tetragonal to orthorhombic phase will have a profound impact on the local $\bar{n}$ of BXT. This is due to the large differences in optical symmetry between the phases. The tetragonal phase will have two indices of refraction while the lower symmetry orthorhombic phase will have three indices. In materials with mixed phase compositions, like polycrystalline BXT, $\bar{n}$ can have contributions from five different refractive indices. The number of refractive indices that are active in BXT will decrease as the phase is homogenized, leading to a significant change in the effective $\bar{n}$. Thus, a transformation from a mixed uniaxial/biaxial composition to a complete biaxial composition will represent a considerable shift in the optical properties, producing a dramatic EO response.

A decrease in the EO effect occurs when the electric field is increased into region III, signifying a change in mechanism. These results correlate well with large-signal piezoelectric measurements conducted by Gao et al [88]. It was found that at electric fields of ~1 MV/m, the slope of the strain-versus-field response in BXT changes abruptly. This change occurs because the ferroelectric/ferroelastic domains are mostly aligned. At this point the domain activity is saturated and therefore domain switching does not significantly contribute to the piezoelectric effect at these large fields. Similarly, the results reported here suggest that the contribution from domain activity to the EO effect is reduced in region III, leading to the decrease in the EO coefficient. It is likely that a more abrupt decrease in the EO response is not observed due to the contribution of the quadratic EO effect (Kerr effect), which is most active at large electric fields.

The EO response to bias field is similar in the increasing and decreasing directions for regions I and III. Deviation occurs in region II, where the EO coefficient plateaus in the decreasing field direction. This suggests that the field induced structural evolution differs between increasing and decreasing field directions. In situ TEM work by Zakhozheva et al. supports this by showing that the single domain state in BXT is not seen while decreasing the electric field [89]. Instead, the high-field multidomain state transitions directly to the zero-field multidomain state, skipping the single domain state entirely.

A schematic of the full proposed structural evolution with electric field is shown in Figure 5.21. At no bias field, BXT is a mix of tetragonal and orthorhombic phases with a multidomain structure (region I). As the applied field is increased, many of the grains form a single domain state while the overall orthorhombic phase content increases (region I and II). A further increase in the electric field strength results in the single domain state transitioning into a multidomain state (region II). At even greater applied fields the domains have finished aligning and the phase transformation has saturated. This results in a saturation of domain activity causing a decreased contribution of domain switching to the EO effect (region III). Upon decreasing the electric field, the single domain state is skipped entirely. At the same time, the orthorhombic phase transitions back to the mixed orthorhombic and tetragonal phase composition. While the above described domain switching and phase conversion are mostly prevalent at large fields, these phenomena are still active at small electric fields and will be the major contributors to the large EO effect observed in BXT. A list summarizing the proposed structural evolution can be seen in Table 5.2.

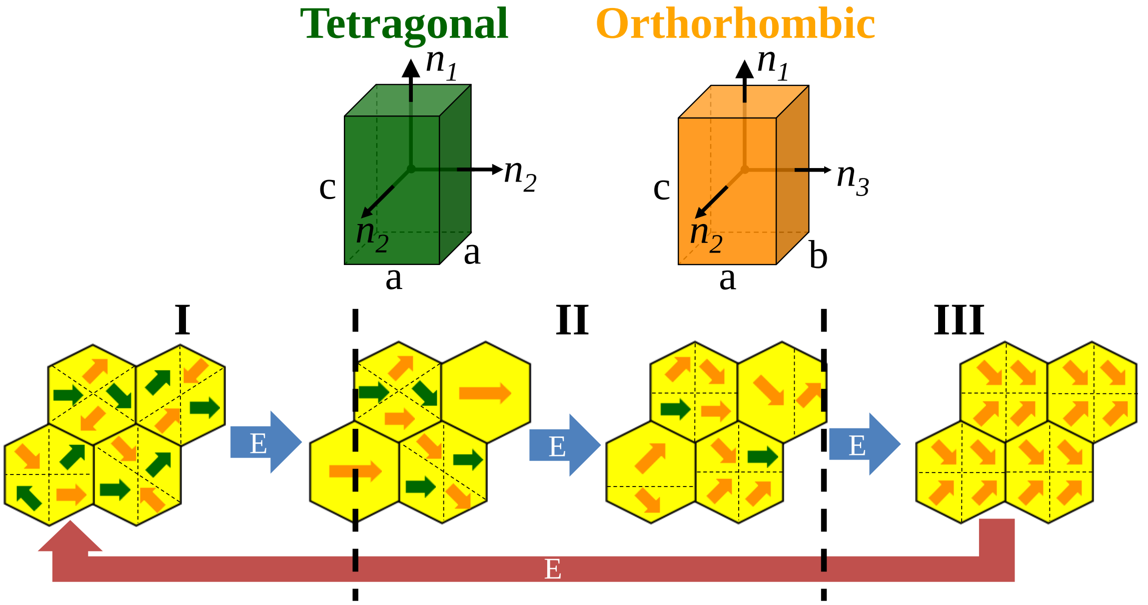

Figure 5.21: Outline of the proposed field induced structural evolution which controls the EO properties of BXT. The color green corresponds to the tetragonal phase, while the color orange corresponds to the orthorhombic phase.

Table 5.2: List summarizing the proposed field induced structural evolution which controls the EO effect in BXT.

Region	**Domain Contribution**	**Phase Contribution**
I	Formation of single domain states	Field induced phase transformation (**O**/**T**→**O**)
II	Break up of single domain states into multidomain states	Continued field induced phase transformation (**O**/**T**→**O**)
III	Saturated domain contribution (domains aligned)	Saturation of **O** Phase
III→I	Direct transition to low field multidomain state	Return to original phase composition (**O**→**O**/**T**)

5.5-Conclusions

Using the new BT based synthesis method and CAPAD processing, polycrystalline BXT was made transparent for the first time. BXT has a remarkably high EO coefficient of r_c = 530 pm/V. Such a large EO coefficient will allow for more compact EO devices that operate using smaller voltages. These advantages could lead to further cost reductions and proliferation of EO technologies.

The large EO response is attributed to a complex electric field induced structural evolution. This evolution consists of a combination of efficient domain motion along with a phase transition to a low symmetry phase. It is likely that similar structural evolutions occur in yet to be discovered materials. The mechanisms explored in this work will be instrumental in the discovery of other high-performance EO materials. The underlying causes of such a structural evolution could provide a framework when searching for other systems with a large EO response.

Perhaps most remarkable is that BXT contains no lead. It is worth noting in particular that BXT is undoped and mostly unoptimized. While materials like PZT have had decades of optimization, BXT still has room to grow. Exploration of different compositions and dopants could improve the EO performance of BXT. In addition, the optical properties of BXT could be further enhanced with more optimized microstructures. BXT based EO devices have the potential to be a safe high performance competitor in a variety of photonics applications.

Chapter 6-Summary and Conclusions

6.1-Summary

EO devices are essential components in a variety of photonics systems. The advancement of EO technology is currently hindered by the challenge associated with developing new EO materials. High performance single crystals are prohibitively difficult to make due to the equilibrium restricted nature of single crystal growth techniques. Thin film EO materials suffer from clamping effects which limit their use in EO devices. Polycrystalline ceramic materials could be a potential source of viable high performance EO materials. While high performance EO ceramic materials like PLZT have been made before, these materials are often lead based and commonly have a slow response time.

The pursuit of lead free electroceramics as an alternative to PZT has resulted in the discovery of a number of promising next generation materials. One of these materials is BXT, which has garnered wide recognition and attention due to its exceptional piezoelectric properties. This material possesses all of the inherent qualities necessary to be an exceptional EO material. Up until this point, however, researchers have not been able to make BXT transparent. Further refinements in the synthesis and processing of BXT will be necessary to make this happen.

In this work it was shown that conventional synthesis methods (BC based) do not provide powders of the necessary quality to make transparent BXT. Even an advanced powder densification technique such as CAPAD requires 1300 °C to form phase pure BXT using BC based synthesis. This temperature is too high to produce the microstructures necessary for optical transparency. A new powder synthesis method was developed (BT based) to ameliorate these issues. This new synthesis technique eliminates the majority of the carbonates found in the BC based method. The BT based synthesis approach combined with CAPAD can produce fully dense, fully reacted, nanocrystalline BXT at temperatures as low as 1000 °C.

When processed in CAPAD at 1200 °C, the BT based synthesis approach allows for the production of transparent BXT polycrystalline ceramics. These ceramics are viable EO materials, with an extraordinary EO coefficient of r_c = 530 pm/V. This is 26.5 times larger than the coefficient for $LiNbO_3$, the current state of the art EO material. Such a high EO coefficient could allow for the significant miniaturization of EO devices and reduction of the power required for operation.

Through careful measurement of the EO properties, it was determined that the EO properties of BXT originate from a complex field induced structural evolution. At zero applied field, BXT has a randomized multidomain structure with a mixture of orthorhombic and tetragonal phases. As the field is increased, BXT adopts a single domain state. Higher fields see the single domain state break up into an ordered multidomain state while the orthorhombic content gradually increases. Further increasing the field strength results in the saturation of the domain state and the phase composition, causing the EO properties to decrease. Decreasing the field strength causes BXT to transition from one multidomain state to another, skipping the single domain state on its way to zero field. This complex structural evolution is the primary contributor to the large EO effect found in BXT.

6.2-Conclusions and Outlook

Synthesis and processing have an enormous impact on the final properties of a densified polycrystalline ceramic. This is due to the effect that these conditions have on the microstructure. The BC based synthesis method does not allow for the microstructures necessary to produce optical transparency in BXT. The complexity of the reaction involved in producing BXT from BC based powders represents a potential source of experimental error. XRD cannot completely verify the completeness of reaction, meaning that some properties of BXT could be being misattributed to other sources.

Switching from BC based synthesis to BT based synthesis has an immediate impact on the densification of BXT. This switch provides 300 °C of additional flexibility in the processing temperature. Changing the synthesis method and using CAPAD processing has allowed for the creation of fully dense, fully reacted, nanocrystalline BXT as well as optically transparent BXT ceramics for the first time. These achievements in processing science have allowed for the first measurements of the optical and EO properties of BXT.

Using the detailed EO measurements shown in this work, it was possible to outline a proposed mechanism for the EO response in BXT. BXT has an unusually complex origin for its ferroelectric phenomena. Observing the EO properties has allowed for optical effects to make a contribution to the current understanding of the ferroelectric mechanisms behind BXT. The mechanism proposed here is the most complete description available for the electric field induced structural evolution found in BXT.

This proposed mechanism could help further the understanding of the ferroelectric properties of BXT. The mechanisms discussed in this work could also provide a framework when searching for other high-performance EO materials.

As the world moves further into the information age, rapid advances in electronic and photonic technologies will be necessary to keep up with the demands of society. Technological advances will require the development of safe and high performance next generation materials. BXT, a product of this century, is a material representing all of the qualities required of next generation materials. It is lead free and non-toxic, allowing it to comply with even the strictest of regulations. It has exceptional ferroelectric properties, with the potential to be implemented in a diverse array of applications. As shown in this work, BXT has incredibly promising EO properties. BXT is a true next generation EO material, with the potential to allow for the safe high performance EO devices that the future requires.

References

[1] S.-E. E. Park and W. Hackenberger, “High performance single crystal piezoelectrics: applications and issues,” *Curr. Opin. Solid State Mater. Sci.*, vol. 6, no. 1, pp. 11–18, Feb. 2002.

[2] X. Wan, H. Luo, X. Zhao, D. Y. Wang, H. L. W. Chan, and C. L. Choy, “Refractive indices and linear electro-optic properties of (1−x)Pb(Mg1/3Nb2/3)O3−xPbTiO3 single crystals,” *Appl. Phys. Lett.*, vol. 85, no. 22, p. 5233, 2004.

[3] B. W. Wessels, “Ferroelectric Epitaxial Thin Films for Integrated Optics,” *Annu. Rev. Mater. Res.*, vol. 37, no. 1, pp. 659–679, Aug. 2007.

[4] N. Setter, D. Damjanovic, L. Eng, G. Fox, S. Gevorgian, S. Hong, A. Kingon, H. Kohlstedt, N. Y. Park, G. B. Stephenson, I. Stolitchnov, A. K. Taganstev, D. V. Taylor, T. Yamada, and S. Streiffer, “Ferroelectric thin films: Review of materials, properties, and applications,” *J. Appl. Phys.*, vol. 100, no. 5, p. 051606, 2006.

[5] F. Griggio, S. Jesse, A. Kumar, O. Ovchinnikov, H. Kim, T. N. Jackson, D. Damjanovic, S. V. Kalinin, and S. Trolier-McKinstry, “Substrate Clamping Effects on Irreversible Domain Wall Dynamics in Lead Zirconate Titanate Thin Films,” *Phys. Rev. Lett.*, vol. 108, no. 15, p. 157604, Apr. 2012.

[6] S. Abel, T. Stöferle, C. Marchiori, C. Rossel, M. D. Rossell, R. Erni, D. Caimi, M. Sousa, A. Chelnokov, B. J. Offrein, and J. Fompeyrine, “A strong electro-optically active lead-free ferroelectric integrated on silicon.,” *Nat. Commun.*, vol. 4, p. 1671, 2013.

[7] P. Tang, A. L. Meier, D. J. Towner, and B. W. Wessels, “BaTiO3 thin-film waveguide modulator with a low voltage-length product at near-infrared wavelengths of 0.98 and 1.55 µm,” *Opt. Lett.*, vol. 30, no. 3, p. 254, Feb. 2005.

[8] Jianheng Li, Zhifu Liu, Yongming Tu, Seng-Tiong Ho, Il Woong Jung, L. E. Ocola, and B. W. Wessels, “Photonic Crystal Waveguide Electro-Optic Modulator With a Wide Bandwidth,” *J. Light. Technol.*, vol. 31, no. 10, pp. 1601–1607, May 2013.

[9] C. . Rosen, B. . Hiremath, and R. Newnham, *Piezoelectricity*. New York, NY: The American Institute of Physics, 1992.

[10] D. Brewster, “Observation on the Pyro-Electricity of Minerals,” *Edinbg. J. Sci.*, vol. I, no. 11, 1824.

[11] J. Curie and P. Curie, “Development by pressure of polar electricity in hemihedral crystals with inclined faces,” *Bull. soc. min. Fr.*, vol. 3, p. 90, 1880.

[12] J. Valasek, “Piezo-Electric and Allied Phenomena in Rochelle Salt,” *Phys. Rev.*, vol. 17, no. 4, pp. 475–481, Apr. 1921.

[13] H. Thurnauer and J. Deaderick, “Insulating material,” 24295881947.

[14] A. von Hippel, R. G. Breckenridge, F. G. Chesley, and L. Tisza, “High dielectric constant ceramics,” *Ind. Eng. Chem.*, vol. 38, no. 11, pp. 1097–1109, Nov. 1946.

[15] W. C. Röntgen, “XIX. On the change in the double refraction of quartz produced by electric forces,” *Philos. Mag. Ser. 5*, vol. 15, no. 92, pp. 132–143, Feb. 1883.

[16] A. Kundt, “Ueber das optische Verhalten des Quarzes im electrischen Felde,” *Ann. Phys. Chem*, vol. 18, pp. 228–233, 1883.

[17] F. Pockels, “Ueber den Einfluss des elektrostatischen Feldes auf das optische Verhalten piëzoelektrischer Krystalle,” *Abh. Gott*, vol. 39, pp. 1–204, 1893.

[18] J. R. Maldonado and A. H. Meitzler, “Ferroelectric domain switching in rhombohedral-phase PLZT ceramics,” *Ferroelectrics*, vol. 3, no. 1, pp. 169–175, Feb. 1972.

[19] C. Pecharromán, G. Mata-Osoro, L. A. Díaz, R. Torrecillas, and J. S. Moya, “On the transparency of nanostructured alumina: Rayleigh-Gans model for anisotropic spheres,” *Opt. Express*, vol. 17, no. 8, p. 6899, Apr. 2009.

[20] E. Cross, “Materials science: Lead-free at last,” *Nature*, vol. 432, no. 7013, pp. 24–25, Nov. 2004.

[21] G. Shirane and A. Takeda, “Phase Transitions in Solid Solutions of PbZrO3 and PbTiO3 Small Concentrations of PbTiO3,” *J. Phys. Soc. Japan*, vol. 7, no. 1, pp. 5–11, Jan. 1952.

[22] B. Jaffe, R. . Roth, and S. Marzullo, “Piezoelectric Properties of Lead Zirconate-Lead Titanate Solid-Solution Ceramics,” *J. Appl. Phys.*, vol. 25, no. 6, p. 809, 1954.

[23] B. Noheda, D. E. Cox, G. Shirane, J. A. Gonzalo, L. E. Cross, and S.-E. Park, “A monoclinic ferroelectric phase in the Pb(Zr1-xTix)O3 solid solution,” *Appl. Phys. Lett.*, vol. 74, no. 14, p. 6, 1999.

[24] D. Damjanovic, “Comments on Origins of Enhanced Piezoelectric Properties in Ferroelectrics,” *IEEE Trans. Ultrason. Ferroelectr. Freq. Control*, vol. 56, no. 8, pp. 1574–1585, Aug. 2009.

[25] N. G. Theofanous, M. Aillerie, M. D. Fontana, and G. E. Alexakis, “A frequency doubling electro-optic modulation system for Pockels effect measurements: Application in LiNbO3,” *Rev. Sci. Instrum.*, vol. 68, no. 5, p. 2138, 1997.

[26] X. Y. Meng, Z. Z. Wang, Y. Zhu, and C. T. Chen, “Mechanism of the electro-optic effect in the perovskite-type ferroelectric KNbO3 and LiNbO3,” *J. Appl. Phys.*, vol. 101, no. 10, p. 103506, 2007.

[27] G. H. HAERTLING and C. E. LAND, “Hot-Pressed (Pb,La)(Zr,Ti)O 3 Ferroelectric Ceramics for Electrooptic Applications,” *J. Am. Ceram. Soc.*, vol. 54, no. 1, pp. 1–11, Jan. 1971.

[28] G. H. Haertling, “PLZT electrooptic materials and applications—a review,” *Ferroelectrics*, vol. 75, no. 1, pp. 25–55, Sep. 1987.

[29] W. Liu and X. Ren, “Large Piezoelectric Effect in Pb-Free Ceramics,” *Phys. Rev. Lett.*, vol. 103, no. 25, pp. 1–4, 2009.

[30] V. S. Puli, D. K. Pradhan, D. B. Chrisey, M. Tomozawa, G. L. Sharma, J. F. Scott, and R. S. Katiyar, “Structure, dielectric, ferroelectric, and energy density properties of (1 − x)BZT–xBCT ceramic capacitors for energy storage applications,” *J. Mater. Sci.*, vol. 48, no. 5, pp. 2151–2157, Mar. 2013.

[31] S. Yao, W. Ren, H. Ji, X. Wu, P. Shi, D. Xue, X. Ren, and Z.-G. Ye, “High pyroelectricity in lead-free 0.5Ba(Zr 0.2 Ti 0.8)O 3 –0.5(Ba 0.7 Ca 0.3)TiO 3 ceramics,” *J. Phys. D. Appl. Phys.*, vol. 45, no. 19, p. 195301, May 2012.

[32] J. Gao, L. Zhang, D. Xue, T. Kimoto, M. Song, L. Zhong, and X. Ren, “Symmetry determination on Pb-free piezoceramic 0.5Ba(Zr0.2Ti0.8)O3-0.5(Ba0.7Ca0.3)TiO3 using convergent beam electron diffraction method,” *J. Appl. Phys.*, vol. 115, no. 5, p. 054108, Feb. 2014.

[33] D. S. Keeble, F. Benabdallah, P. A. Thomas, M. Maglione, and J. Kreisel, “Revised structural phase diagram of (Ba0.7Ca0.3TiO3)-(BaZr0.2Ti0.8O3),” *Appl. Phys. Lett.*, vol. 102, no. 9, p. 092903, 2013.

[34] G. Singh, A. Upadhaya, A. K. Sinha, and V. S. Tiwari, “Investigation of orthorhombic–tetragonal structural crossover in (Ba 0.92 Ca 0.08)(Zr 0.05 Ti 0.95)O 3,” *J. Appl. Crystallogr.*, vol. 47, no. 5, pp. 1647–1650, Oct. 2014.

[35] F. Cordero, F. Craciun, M. Dinescu, N. Scarisoreanu, C. Galassi, W. Schranz, and V. Soprunyuk, "Elastic response of (1 − x)Ba(Ti0.8Zr0.2)O3 – x(Ba0.7Ca0.3)TiO3 (x = 0.45–0.55) and the role of the intermediate orthorhombic phase in enhancing the piezoelectric coupling," *Appl. Phys. Lett.*, vol. 105, no. 23, p. 232904, Dec. 2014.

[36] M. McQUARRIE and F. W. BEHNKE, "Structural and Dielectric Studies in the System (Ba, Ca) (Ti, Zr)O3," *J. Am. Ceram. Soc.*, vol. 37, no. 11, pp. 539–543, Nov. 1954.

[37] K. Mimura, T. Naka, T. Shimura, W. Sakamoto, and T. Yogo, "Synthesis and dielectric properties of (Ba,Ca)(Zr,Ti)O3 thin films using metal-organic precursor solutions," *Thin Solid Films*, vol. 516, no. 23, pp. 8408–8413, Oct. 2008.

[38] X.-G. Tang and H. L.-W. Chan, "Effect of grain size on the electrical properties of (Ba,Ca)(Zr,Ti)O3 relaxor ferroelectric ceramics," *J. Appl. Phys.*, vol. 97, no. 3, p. 034109, 2005.

[39] Xingwei Yan, Kwok Ho Lam, Xiang Li, Ruimin Chen, Wei Ren, Xiaobing Ren, Qifa Zhou, and K. K. Shung, "Correspondence: Lead-free intravascular ultrasound transducer using BZT-50BCT ceramics," *IEEE Trans. Ultrason. Ferroelectr. Freq. Control*, vol. 60, no. 6, pp. 1272–1276, Jun. 2013.

[40] R. L. Coble, "Transparent alumina and method of preparation." Google Patents, 1962.

[41] J. E. Garay, "Current-Activated, Pressure-Assisted Densification of Materials," *Annu. Rev. Mater. Res.*, vol. 40, no. 1, pp. 445–468, Jul. 2010.

[42] R. Orrù, R. Licheri, A. M. Locci, A. Cincotti, and G. Cao, "Consolidation/synthesis of materials by electric current activated/assisted sintering," *Mater. Sci. Eng. R Reports*, vol. 63, no. 4–6, pp. 127–287, Feb. 2009.

[43] F. Maglia, I. G. Tredici, and U. Anselmi-Tamburini, "Densification and properties of bulk nanocrystalline functional ceramics with grain size below 50nm," *J. Eur. Ceram. Soc.*, vol. 33, no. 6, pp. 1045–1066, Jun. 2013.

[44] U. Anselmi-Tamburini, J. E. Garay, and Z. A. Munir, "Fast low-temperature consolidation of bulk nanometric ceramic materials," *Scr. Mater.*, vol. 54, no. 5, pp. 823–828, Mar. 2006.

[45] T. Hungría, J. Galy, and A. Castro, "Spark Plasma Sintering as a Useful Technique to the Nanostructuration of Piezo-Ferroelectric Materials," *Adv. Eng. Mater.*, vol.

11, no. 8, pp. 615–631, 2009.

[46] Y. Kodera, C. L. Hardin, and J. E. Garay, “Transmitting, emitting and controlling light: Processing of transparent ceramics using current-activated pressure-assisted densification,” *Scr. Mater.*, vol. 69, no. 2, pp. 149–154, Jul. 2013.

[47] J. E. Alaniz, A. D. Dupuy, Y. Kodera, and J. E. Garay, “Effects of applied pressure on the densification rates in current-activated pressure-assisted densification (CAPAD) of nanocrystalline materials,” *Scr. Mater.*, vol. 92, pp. 7–10, Dec. 2014.

[48] U. Anselmi-Tamburini, J. E. Garay, and Z. A. Munir, “Fundamental investigations on the spark plasma sintering/synthesis process: III. Current effect on reactivity,” *Mater. Sci. Eng. A*, vol. 407, no. 1–2, pp. 24–30, 2005.

[49] E. H. Penilla, Y. Kodera, and J. E. Garay, “Blue-Green Emission in Terbium-Doped Alumina (Tb:Al 2 O 3) Transparent Ceramics,” *Adv. Funct. Mater.*, vol. 23, no. 48, pp. 6036–6043, Dec. 2013.

[50] C. B. Sawyer and C. H. Tower, “Rochelle Salt as a Dielectric,” *Phys. Rev.*, vol. 35, no. 3, pp. 269–273, Feb. 1930.

[51] H. de Sénarmont, “Sur les modifications que la réflexion spéculaire à la surface des corps métalliques imprime à un rayon de lumière polarisée,” *Ann. Chim. Phys*, vol. 73, pp. 337–62, 1840.

[52] P. Tang, D. J. Towner, A. L. Meier, and B. W. Wessels, “Low-voltage, polarization-insensitive, electro-optic modulator based on a polydomain barium titanate thin film,” *Appl. Phys. Lett.*, vol. 85, no. 20, p. 4615, 2004.

[53] L. K. TEMPLETON and J. A. PASK, “Formation of BaTiO3 from BaCO3 and TiO2 in Air and in CO2,” *J. Am. Ceram. Soc.*, vol. 42, no. 5, pp. 212–216, May 1959.

[54] M. T. Buscaglia, M. Bassoli, V. Buscaglia, and R. Alessio, “Solid-State Synthesis of Ultrafine BaTiO3 Powders from Nanocrystalline BaCO3 and TiO2,” *J. Am. Ceram. Soc.*, vol. 88, no. 9, pp. 2374–2379, Sep. 2005.

[55] J. Paul Praveen, K. Kumar, A. R. James, T. Karthik, S. Asthana, and D. Das, “Large piezoelectric strain observed in sol-gel derived BZT-BCT ceramics,” *Curr. Appl. Phys.*, vol. 14, no. 3, pp. 396–402, Jan. 2014.

[56] V. S. Puli, A. Kumar, D. B. Chrisey, M. Tomozawa, J. F. Scott, and R. S. Katiyar, “Barium zirconate-titanate/barium calcium-titanate ceramics via sol–gel process:

novel high-energy-density capacitors," *J. Phys. D. Appl. Phys.*, vol. 44, no. 39, p. 395403, Oct. 2011.

[57] G. K. Sahoo and R. Mazumder, "Low temperature synthesis of Ba(Zr0.2Ti0.8)O3–0.5(Ba0.7Ca0.3)TiO3 nanopowders by solution based auto combustion method," *J. Mater. Sci. Mater. Electron.*, vol. 25, no. 8, pp. 3515–3519, Aug. 2014.

[58] P. Mishra, Sonia, and P. Kumar, "Effect of sintering temperature on dielectric, piezoelectric and ferroelectric properties of BZT–BCT 50/50 ceramics," *J. Alloys Compd.*, vol. 545, pp. 210–215, Dec. 2012.

[59] J. Liu, Z. Shen, W. Yao, Y. Zhao, and A. K. Mukherjee, "Visible and infrared transparency in lead-free bulk BaTiO(3) and SrTiO(3) nanoceramics.," *Nanotechnology*, vol. 21, no. 7, p. 75706, Feb. 2010.

[60] J. Hao, W. Bai, W. Li, and J. Zhai, "Correlation Between the Microstructure and Electrical Properties in High-Performance (Ba0.85Ca0.15)(Zr0.1Ti0.9)O3 Lead-Free Piezoelectric Ceramics," *J. Am. Ceram. Soc.*, vol. 95, no. 6, pp. 1998–2006, Jun. 2012.

[61] K. OKAZAKI and K. NAGATA, "Effects of Grain Size and Porosity on Electrical and Optical Properties of PLZT Ceramics," *J. Am. Ceram. Soc.*, vol. 56, no. 2, pp. 82–86, Feb. 1973.

[62] L. Lutterotti, M. Bortolotti, G. Ischia, I. Lonardelli, and H.-R. Wenk, "Rietveld texture analysis from diffraction images," *Zeitschrift für Krist. Suppl.*, vol. 26, pp. 125–130, Nov. 2007.

[63] D. L. Wood and J. Tauc, "Weak Absorption Tails in Amorphous Semiconductors," *Phys. Rev. B*, vol. 5, no. 8, pp. 3144–3151, Apr. 1972.

[64] M. DiDomenico and S. H. Wemple, "Oxygen-octahedra ferroelectrics. I. Theory of electro-optical and nonlinear optical effects," *J. Appl. Phys.*, vol. 40, no. 2, pp. 720–734, 1969.

[65] S. H. Wemple, M. Didomenico, and I. Camlibel, "Dielectric and optical properties of melt-grown BaTiO3," *J. Phys. Chem. Solids*, vol. 29, no. 10, pp. 1797–1803, Oct. 1968.

[66] P. D. Thacher, "A linear electrooptic effect in ferroelectric ceramics: PLZT 12/40/60," *Ferroelectrics*, vol. 3, no. 1, pp. 147–156, Feb. 1972.

[67] D. E. Zelmon, D. L. Small, and D. Jundt, "Infrared corrected Sellmeier coefficients

for congruently grown lithium niobate and 5 mol.% magnesium oxide –doped lithium niobate," *J. Opt. Soc. Am. B*, vol. 14, no. 12, p. 3319, Dec. 1997.

[68] B. Li, J. E. Blendell, and K. J. Bowman, "Temperature-Dependent Poling Behavior of Lead-free BZT-BCT Piezoelectrics," *J. Am. Ceram. Soc.*, vol. 94, no. 10, pp. 3192–3194, Jul. 2011.

[69] M. C. Ehmke, J. Glaum, M. Hoffman, J. E. Blendell, and K. J. Bowman, "The Effect of Electric Poling on the Performance of Lead-Free (1− x)Ba(Zr 0.2 Ti 0.8)O 3 - x (Ba 0.7 Ca 0.3)TiO 3 Piezoceramics," *J. Am. Ceram. Soc.*, vol. 96, no. 12, pp. 3805–3811, Dec. 2013.

[70] J. P. Praveen, T. Karthik, A. R. James, E. Chandrakala, S. Asthana, and D. Das, "Effect of poling process on piezoelectric properties of sol–gel derived BZT–BCT ceramics," *J. Eur. Ceram. Soc.*, vol. 35, no. 6, pp. 1785–1798, 2015.

[71] H. Li, Y. Zhang, J. Wen, S. Yang, D. Mo, C.-H. Cheng, Y. Xu, and J. D. Mackenzie, "Optical Properties of Lead Lanthanum Zirconate Titanate Amorphous Ferroelectric-Like Thin Films," *Jpn. J. Appl. Phys.*, vol. 39, no. Part 1, No. 3A, pp. 1180–1183, Mar. 2000.

[72] D. Redfield and W. J. Burke, "Optical absorption edge of LiNbO3," *J. Appl. Phys.*, vol. 45, no. 10, p. 4566, 1974.

[73] S. H. Wemple, "Polarization fluctuations and the optical-absorption edge in BaTiO3," *Phys. Rev. B*, vol. 2, no. 7, pp. 2679–2689, 1970.

[74] J. E. Alaniz, F. G. Perez-Gutierrez, G. Aguilar, and J. E. Garay, "Optical properties of transparent nanocrystalline yttria stabilized zirconia," *Opt. Mater. (Amst).*, vol. 32, no. 1, pp. 62–68, Nov. 2009.

[75] E. H. Penilla, C. L. Hardin, Y. Kodera, S. A. Basun, D. R. Evans, and J. E. Garay, "The role of scattering and absorption on the optical properties of birefringent polycrystalline ceramics: Modeling and experiments on ruby (Cr:Al2O3)," *J. Appl. Phys.*, vol. 119, no. 2, p. 023106, Jan. 2016.

[76] K. Uchino, "Electro-optic ceramics and their display applications," *Ceram. Int.*, vol. 21, no. 5, pp. 309–315, 1995.

[77] F. S. Chen, "Evaluation of PLZT ceramics for applications in optical communications," *Opt. Commun.*, vol. 6, no. 3, pp. 297–300, Nov. 1972.

[78] D. M. Gill, C. W. Conrad, G. Ford, B. W. Wessels, and S. T. Ho, "Thin-film

channel waveguide electro-optic modulator in epitaxial BaTiO3,” *Appl. Phys. Lett.*, vol. 71, no. 13, p. 1783, 1997.

[79] A. R. Johnston, “Dispersion of Electro-Optic Effect in BaTiO3,” *J. Appl. Phys.*, vol. 42, no. 9, p. 3501, 1971.

[80] M. Abarkan, J. P. Salvestrini, M. D. Fontana, and M. Aillerie, “Frequency and wavelength dependences of electro-optic coefficients in inorganic crystals,” *Appl. Phys. B Lasers Opt.*, vol. 76, no. 7, pp. 765–769, Jul. 2003.

[81] G. H. Haertling and C. E. Land, “Recent improvements in the optical and electrooptic properties of plzt ceramics,” *Ferroelectrics*, vol. 3, no. 1, pp. 269–280, Feb. 1972.

[82] M. Buscaglia, M. Viviani, V. Buscaglia, L. Mitoseriu, A. Testino, P. Nanni, Z. Zhao, M. Nygren, C. Harnagea, D. Piazza, and C. Galassi, “High dielectric constant and frozen macroscopic polarization in dense nanocrystalline BaTiO3 ceramics,” *Phys. Rev. B*, vol. 73, no. 6, p. 064114, Feb. 2006.

[83] H. Guo, C. Zhou, X. Ren, and X. Tan, “Unique single-domain state in a polycrystalline ferroelectric ceramic,” *Phys. Rev. B*, vol. 89, no. 10, p. 100104, Mar. 2014.

[84] M. Acosta, N. Novak, G. A. Rossetti, and J. Rödel, “Mechanisms of electromechanical response in (1 − x)Ba(Zr0.2Ti0.8)O3-x(Ba0.7Ca0.3)TiO3 ceramics,” *Appl. Phys. Lett.*, vol. 107, no. 14, p. 142906, Oct. 2015.

[85] H. Guo, B. K. Voas, S. Zhang, C. Zhou, X. Ren, S. P. Beckman, and X. Tan, “Polarization alignment, phase transition, and piezoelectricity development in polycrystalline 0.5Ba(Zr0.2Ti0.8)O3−0.5(Ba0.7Ca0.3)TiO3,” *Phys. Rev. B*, vol. 90, no. 1, p. 014103, Jul. 2014.

[86] M. Hinterstein, J. Rouquette, J. Haines, P. Papet, M. Knapp, J. Glaum, and H. Fuess, “Structural Description of the Macroscopic Piezo- and Ferroelectric Properties of Lead Zirconate Titanate,” *Phys. Rev. Lett.*, vol. 107, no. 7, p. 077602, Aug. 2011.

[87] H. Guo, S. Zhang, S. P. Beckman, and X. Tan, “Microstructural origin for the piezoelectricity evolution in (K0.5Na0.5)NbO3-based lead-free ceramics,” *J. Appl. Phys.*, vol. 114, no. 15, p. 154102, 2013.

[88] J. Gao, X. Hu, L. Zhang, F. Li, L. Zhang, Y. Wang, Y. Hao, L. Zhong, and X. Ren, “Major contributor to the large piezoelectric response in (1 − x)Ba(Zr0.2Ti0.8)O3

− x(Ba0.7Ca0.3)TiO3 ceramics: Domain wall motion," *Appl. Phys. Lett.*, vol. 104, no. 25, p. 252909, Jun. 2014.

[89] M. Zakhozheva, L. A. Schmitt, M. Acosta, H. Guo, W. Jo, R. Schierholz, H.-J. Kleebe, and X. Tan, "Wide Compositional Range In Situ Electric Field Investigations on Lead-Free Ba (Zr 0.2 Ti 0.8) O 3 − x (Ba 0.7 Ca 0.3) TiO 3 Piezoceramic," *Phys. Rev. Appl.*, vol. 3, no. 6, p. 064018, Jun. 2015.